

THE EVOLUTION OF THE STELLAR MASS FUNCTIONS OF STAR-FORMING AND QUIESCENT GALAXIES TO $z = 4$ FROM THE COSMOS/UltraVISTA SURVEY*

ADAM MUZZIN¹, DANILO MARCHESEINI², MAURO STEFANON³, MARIJN FRANX¹, HENRY J. McCracken⁴, BO MILVANG-JENSEN⁵, JAMES S. DUNLOP⁶, J. P. U. FYNBO⁵, GABRIEL BRAMMER⁷, IVO LABBÉ¹, AND PIETER G. VAN DOKKUM⁸

¹ Leiden Observatory, Leiden University, P.O. Box 9513, 2300 RA Leiden, The Netherlands

² Department of Physics and Astronomy, Tufts University, Medford, MA 02150, USA

³ Physics and Astronomy Department, University of Missouri, Columbia, MO 65211, USA

⁴ Institut d’Astrophysique de Paris, UMR7095 CNRS, Université Pierre et Marie Curie, 98 bis Boulevard Arago, F-75014 Paris, France

⁵ Dark Cosmology Centre, Niels Bohr Institute, University of Copenhagen, Juliane Maries Vej 30, DK-2100 Copenhagen, Denmark

⁶ SUPA, Institute for Astronomy, University of Edinburgh, Royal Observatory, Edinburgh EH9 3HJ, UK

⁷ European Southern Observatory, Alonso de Córdova 3107, Casilla 19001, Vitacura, Santiago, Chile

⁸ Department of Astronomy, Yale University, New Haven, CT 06520-8101, USA

Received 2013 March 18; accepted 2013 August 14; published 2013 October 9

ABSTRACT

We present measurements of the stellar mass functions (SMFs) of star-forming and quiescent galaxies to $z = 4$ using a sample of 95,675 K_s -selected galaxies in the COSMOS/UltraVISTA field. The SMFs of the combined population are in good agreement with previous measurements and show that the stellar mass density of the universe was only 50%, 10%, and 1% of its current value at $z \sim 0.75$, 2.0, and 3.5, respectively. The quiescent population drives most of the overall growth, with the stellar mass density of these galaxies increasing as $\rho_{\text{star}} \propto (1+z)^{-4.7 \pm 0.4}$ since $z = 3.5$, whereas the mass density of star-forming galaxies increases as $\rho_{\text{star}} \propto (1+z)^{-2.3 \pm 0.2}$. At $z > 2.5$, star-forming galaxies dominate the total SMF at all stellar masses, although a non-zero population of quiescent galaxies persists to $z = 4$. Comparisons of the K_s -selected star-forming galaxy SMFs with UV-selected SMFs at $2.5 < z < 4$ show reasonable agreement and suggest that UV-selected samples are representative of the majority of the stellar mass density at $z > 3.5$. We estimate the average mass growth of individual galaxies by selecting galaxies at fixed cumulative number density. The average galaxy with $\log(M_{\text{star}}/M_{\odot}) = 11.5$ at $z = 0.3$ has grown in mass by only 0.2 dex (0.3 dex) since $z = 2.0$ (3.5), whereas those with $\log(M_{\text{star}}/M_{\odot}) = 10.5$ have grown by >1.0 dex since $z = 2$. At $z < 2$, the time derivatives of the mass growth are always larger for lower-mass galaxies, which demonstrates that the mass growth in galaxies since that redshift is mass-dependent and primarily bottom-up. Lastly, we examine potential sources of systematic uncertainties in the SMFs and find that those from photo- z templates, stellar population synthesis modeling, and the definition of quiescent galaxies dominate the total error budget in the SMFs.

Key words: galaxies: evolution – galaxies: fundamental parameters – galaxies: high-redshift – galaxies: luminosity function, mass function

Online-only material: color figures, machine-readable tables

1. INTRODUCTION

In the current Λ CDM paradigm, the dominant structures in the universe are dark matter halos that grow out of an initial field of density perturbations via gravitational collapse (White & Rees 1978). Simulations and analytical models show that this process proceeds primarily in a hierarchical, bottom-up manner, with low-mass halos forming early and subsequently growing via continued accretion and merging to form more massive halos at later times (White & Frenk 1991; Kauffmann & White 1993; Kauffmann et al. 1999).

In contrast with the predicted hierarchical growth of the dark matter halos, observational studies suggest that the stellar baryonic component of the halos (i.e., galaxies) may grow in an anti-hierarchical, top-down manner. It appears that many of the most massive galaxies ($\log(M_{\text{star}}/M_{\odot}) > 11$) in the local universe assembled their stellar mass rapidly and at early times ($z > 2$), whereas lower mass galaxies grew more gradually over cosmic time (e.g., Marchesini et al. 2009, 2010; Ilbert et al. 2010; Caputi et al. 2011; Brammer et al. 2011).

Understanding these apparently contrasting evolutionary paths for the dark matter assembly and stellar mass assembly of galaxies is a significant challenge for current models of galaxy formation (e.g., Marchesini et al. 2009; Fontanot et al. 2009). In particular, the differential evolution between the baryonic and non-baryonic components of galaxies makes it clear that the baryonic physics of galaxy formation must be more complex than the cooling of gas onto halos at a rate dictated by gravity. Indeed, it implies that there is a tenuous balance between gas accretion rates, gas consumption rates (in both star formation events and black hole growth), mergers, as well as feedback processes such as active galactic nucleus (AGN) activity, supernovae, or stellar winds. It is also clear that the efficiency of these processes must scale with halo mass and evolve with redshift (e.g., Schaye et al. 2010; Weinmann et al. 2012; Henriques et al. 2013). Given the complex, nonlinear interplay between these processes and the various possible prescriptions of implementing them within models, it is important to have a benchmark for the models so that we can evaluate if progress is being made.

For cosmological simulations, the benchmark that has been most widely adopted is the ability of models to match the volume density of galaxies as function of their stellar mass, also known as the stellar mass function (hereafter, SMF). If a model can reproduce the SMFs at various redshifts it suggests (although

* Based on data products from observations made with ESO Telescopes at the La Silla Paranal Observatory under ESO programme ID 179.A-2005 and on data products produced by TERAPIX and the Cambridge Astronomy Survey Unit on behalf of the UltraVISTA consortium.

does not prove) that it may be a better description of the baryonic physics of galaxy formation than those that do not. Given that it is a key benchmark for models, the most precise and accurate measurements possible of the SMF over as large a range in redshift and stellar mass are valuable quantities.

In recent years, with the growth of deep and wide-field near infrared (NIR) imaging surveys, there have been myriad measurements of the evolution of the SMFs from the local universe (e.g., Cole et al. 2001; Bell et al. 2003; Li & White 2009; Baldry et al. 2012) up to $z = 2\text{--}5$ (e.g., Drory et al. 2005; Bundy et al. 2006; Pozzetti et al. 2007; Arnouts et al. 2007; Pérez-González et al. 2008; Drory et al. 2009; Marchesini et al. 2009, 2010; Ilbert et al. 2010; Pozzetti et al. 2010; Domínguez Sánchez et al. 2011; Bielby et al. 2012; Moustakas et al. 2013; Ilbert et al. 2013). In this paper, we present an improved measurement of the SMF of galaxies over the redshift range $0.2 < z < 4.0$. These measurements are made from a new K_s -selected catalog of the COSMOS field, which uses data from the DR1 UltraVISTA survey (see McCracken et al. 2012). The UltraVISTA catalog is unique in its combination of covering a wide area (1.62 deg^2) to a relatively deep depth ($K_{s,\text{tot}} < 23.4$, 90% completeness). This combination allows the most accurate measurements of the high-mass end of the SMFs up to $z = 4.0$ to date. Details of the catalog and a public release of all catalog data products are presented in a companion paper by Muzzin et al. (2013).

We note that an independent analysis of the SMFs out to $z = 4$ using the UltraVISTA data has also recently been performed by Ilbert et al. (2013). That analysis is based on a different catalog than that of the Muzzin et al. (2013) and uses different photometric redshift and stellar mass fitting techniques. In Appendices A and B, we make a more detailed comparison between our SMFs and those derived by Ilbert et al. (2013).

The layout of this paper is as follows. In Section 2, we present details of the COSMOS/UltraVISTA dataset and discuss the stellar mass and photometric redshift measurements. In Section 3, we detail how the SMFs and the uncertainties are calculated. In Section 4, we derive the SMFs of star-forming and quiescent galaxies and the stellar mass density (SMD) and number density evolution up to $z = 4$. In Section 5, we present a discussion of our results, including a comparison with UV-selected SMFs at $z > 3$ and an estimation of the typical mass growth of galaxies using a fixed cumulative number density approach. We conclude in Section 6 with a summary of our results. In Appendices A and B, we present a detailed look at possible sources of systematic error and their effect on the derived SMFs. Throughout this paper, we assume a $\Omega_\Lambda = 0.7$, $\Omega_m = 0.3$, and $H_0 = 70 \text{ km s}^{-1} \text{ Mpc}^{-1}$ cosmology. All magnitudes are in the AB system.

2. THE DATASET

This study is based on a K_s -selected catalog of the COSMOS/UltraVISTA field from Muzzin et al. (2013). The catalog contains point-spread function (PSF) matched photometry in 30 photometric bands covering the wavelength range $0.15\text{--}24 \mu\text{m}$ and includes the available *GALEX* (Martin et al. 2005), CFHT/Subaru (Capak et al. 2007), UltraVISTA (McCracken et al. 2012), and S-COSMOS (Sanders et al. 2007) datasets. Sources are selected from the DR1 UltraVISTA K_s -band imaging (McCracken et al. 2012), which reaches a depth of $K_{s,\text{tot}} < 23.4$ at 90% completeness. A detailed description of the photometric catalog construction, photometric redshift (z_{phot}) measurements, and stellar mass (hereafter, M_{\star}) esti-

mates is presented in Muzzin et al. (2013). A public release of all data products from the catalog is also presented with that paper. Here, we briefly describe the aspects of the catalog relevant to the measurement of the SMFs.

2.1. Photometric Redshifts and Stellar Masses

Each galaxy in the catalog has a z_{phot} determined by fitting the photometry in the $0.15\text{--}8.0 \mu\text{m}$ bands to template spectral energy distributions (SEDs) using the EAZY code (Brammer et al. 2008). In default mode, EAZY fits photometric redshifts using linear combinations of six templates from the PEGASE models (Fioc & Rocca-Volmerange 1999), as well as an additional red template from the Maraston (2005) models. In order to improve the accuracy of the z_{phot} values for high-redshift galaxies, we added two new templates to the default set; a ~ 1 Gyr old post-starburst template, as well as a slightly dust-reddened Lyman break template (see Muzzin et al. 2013). Comparison of the z_{phot} values with 5100 spectroscopic redshifts from the zCOSMOS-bright 10k sample (Lilly et al. 2007), as well as 19 spectroscopic redshifts for red galaxies at $z > 1$ (van de Sande et al. 2011, 2013; Onodera et al. 2012; Bezanson et al. 2013) shows that the z_{phot} values have an rms dispersion of $\delta z/(1+z) = 0.013$ and a $>3\sigma$ catastrophic outlier fraction of 1.6%.

Stellar masses for all galaxies have been determined by fitting the SEDs of galaxies to stellar population synthesis (SPS) models using the FAST code (Kriek et al. 2009). It is well known that M_{\star} derived from SED fitting depends on the assumptions made (metallicity, SPS model, dust law, initial mass function (IMF)) in this process (e.g., Marchesini et al. 2009; Muzzin et al. 2009a, 2009b; Conroy et al. 2009). These assumptions typically result in systematic changes to the SMFs, rather than larger random errors (e.g., Marchesini et al. 2009). Given the complexity of these systematic dependencies, in this paper we base the majority of the analysis on a default set of assumptions for the SED modeling and then in Appendix A we expand the range of SED modeling parameter space and explore the effects on the SMFs. In Appendix A, we also explore the effects of expanding the EAZY template set to include an old and dusty template, which provides a good fit for some of the bright high-redshift population (see also Marchesini et al. 2010).

For the default set of M_{\star} we fit the SEDs to a set of models with exponentially declining star formation histories (SFHs) of the form $\text{SFR} \propto e^{-t/\tau}$, where t is the time since the onset of star formation, and τ sets the timescale of the decline in the star formation rate (SFR). We use the models of Bruzual & Charlot (2003), hereafter BC03, with solar metallicity, a Calzetti et al. (2000) dust law, and we assume a Kroupa (2001) IMF.⁹ We allow $\log(\tau/\text{Gyr})$ to range between 7.0 and 10.0, $\log(t/\text{Gyr})$ to range between 7.0 and 10.1, and A_v to range between 0 and 4. The maximum allowed age of galaxies is set by the age of the universe at their z_{phot} . Further details on the default model set and the fitting process are discussed in Muzzin et al. (2013).

3. CONSTRUCTION OF THE STELLAR MASS FUNCTIONS

Here, we outline how the SMFs for the quiescent, star forming, and combined populations are constructed.

⁹ The stellar masses in the Muzzin et al. (2013) catalog are computed with a Chabrier (2003) IMF. For easy comparison with the literature, we have converted them to a Kroupa (2001) IMF by increasing them by 0.04 dex.

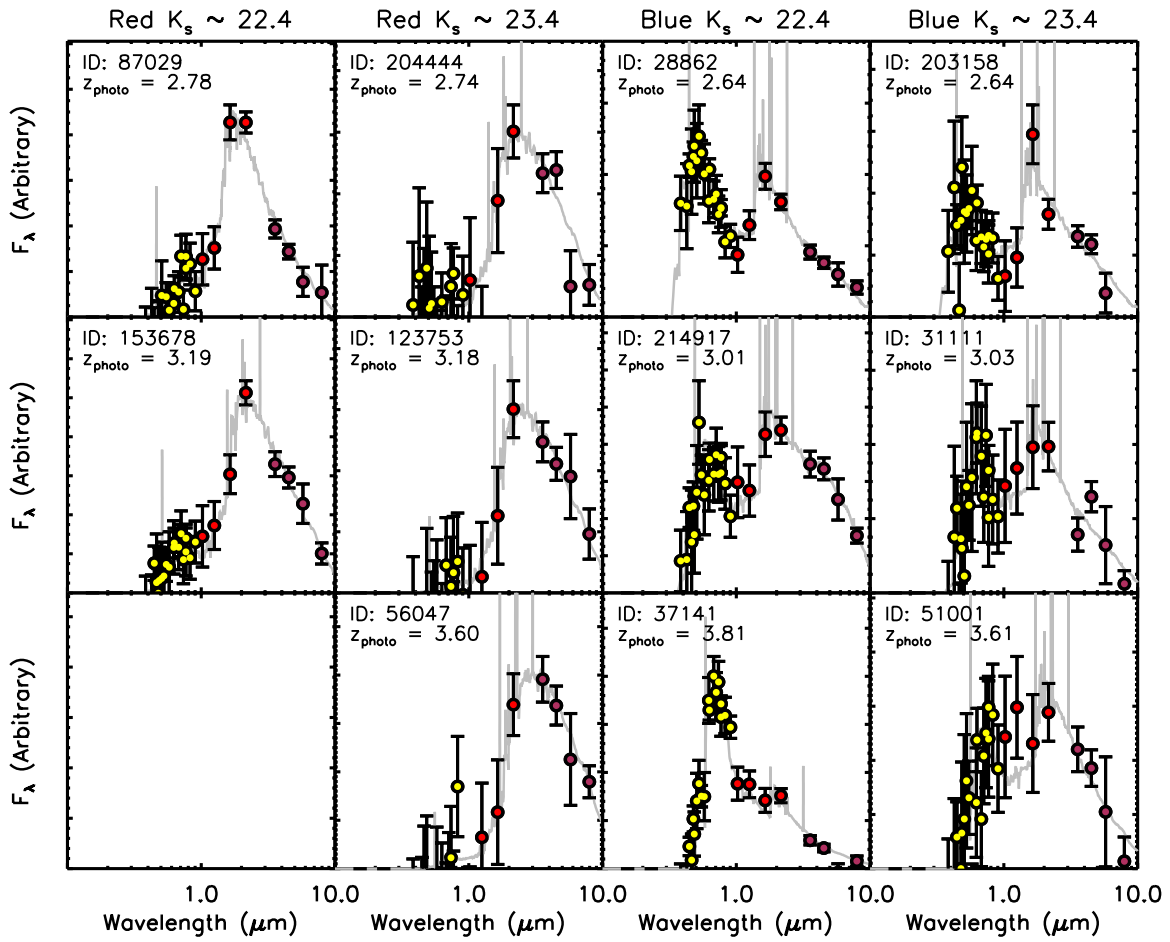


Figure 1. Example SEDs from EAZY of red and blue galaxies in three redshift ranges: $2.5 < z < 3.0$ (top row), $3.0 < z < 3.5$ (middle row), and $3.5 < z < 4.0$ (bottom row). The second and fourth columns show galaxies that have magnitudes near the limiting magnitude of the SMFs ($K_s \sim 23.4$) and the first and third columns show galaxies that are ~ 1 mag brighter. There are no red galaxies with $K_s \sim 22.4$ at $3.5 < z < 4.0$. The SEDs of galaxies at the $K_s = 23.4$ limit typically have $S/N \sim 5$ and therefore we have limited the SMFs to a limiting M_{\star} that corresponds to this limit.

(A color version of this figure is available in the online journal.)

3.1. Galaxy Sample and Completeness

The Muzzin et al. (2013) catalog contains a total of 262,615 objects down to a 3σ limit of $K_s < 24.35$ in a $2''1$ aperture. From that parent sample, we define a mass-complete sample for computing the SMFs by applying various cuts to the catalog.

Simulations of the catalog completeness (see Muzzin et al. 2013, Figure 4) show that the 90% point-source completeness limit in total magnitudes for the UltraVISTA data is $K_{s,\text{tot}} = 23.4$ after source blending is accounted for. This limit in $K_{s,\text{tot}}$ also corresponds to the $\sim 5\sigma$ limit for the photometry in the $2''1$ color aperture, and therefore is a sensible limiting magnitude for computing the SMFs.

As a demonstration of the quality of the SEDs near the 90% completeness limit, we plot in Figure 1 some randomly chosen examples of red and blue galaxy SEDs in three redshift bins: $2.5 < z < 3.0$ (top row), $3.0 < z < 3.5$ (middle row), and $3.5 < z < 4.0$ (bottom row). We plot SEDs of galaxies that have fluxes near the 90% completeness limit ($K_{s,\text{tot}} \sim 23.4$), as well as SEDs of galaxies that are ~ 1 magnitude brighter ($K_{s,\text{tot}} \sim 22.4$). Figure 1 shows that the SEDs of both red and blue galaxies at $K_{s,\text{tot}} \sim 22.4$ are very well constrained. It also shows that at $K_{s,\text{tot}} \sim 23.4$, the SEDs are also reasonably well constrained; however, the typical signal-to-noise ratio (S/N) in a $2''1$ aperture is ~ 5 .

It is possible to include galaxies fainter than the 90% $K_{s,\text{tot}}$ completeness limit in the SMFs and correct for this incompleteness; however, given that the quality of the SEDs near $K_{s,\text{tot}} \sim 23.4$ becomes marginal, we have chosen to restrict the sample to galaxies with good S/N photometry. This ensures that all galaxies included in the SMFs have reasonably well determined M_{\star} and z_{phot} values.

When constructing the SMFs, we also exclude objects flagged as stars ($\text{star} = 1$) based on a color–color cut, as well as those with badly contaminated photometry (SExtractor flag $K_{\text{flag}} > 4$). Objects nearby very bright stars ($\text{contamination} = 1$) or bad regions ($\text{nan_contam} > 3$) are also excluded, and the reduction in area from these effects is taken account into the total survey volume.

Once these cuts are applied, the final sample of galaxies available for the analysis is 160,070. In Figure 2, we plot a grayscale representation of the M_{\star} of this sample as a function of z_{phot} . In general, the sample is dominated by objects at $z < 2$; however, there are reliable sources out to $z = 4$.

3.2. Stellar Mass Completeness versus z

Figure 2 shows the M_{\star} of galaxies down to 90% K_s -band completeness limit of the survey; however, in order to construct the SMFs, the limiting M_{\star} above which the magnitude-limited sample is complete needs to be determined.

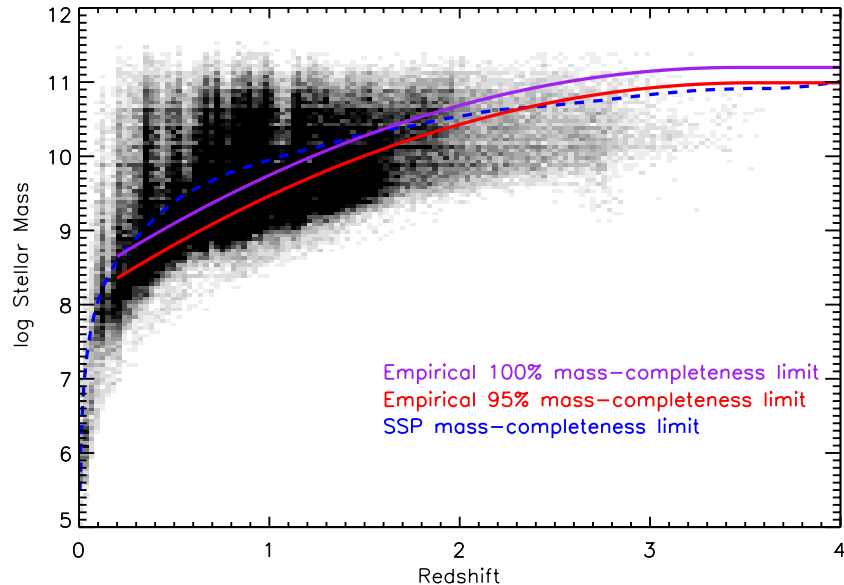


Figure 2. Grayscale representation of the density of galaxy stellar masses as a function of redshift in the K_s -selected catalog. The 100% and 95% mass completeness limits determined using the deeper datasets are shown as the purple and red curves, respectively. Also shown is the 100% completeness limit for a SSP formed at $z = 10$.

(A color version of this figure is available in the online journal.)

In order to estimate the redshift-dependent completeness limit in M_{star} , we adopt the approach developed in Marchesini et al. (2009), which exploits the availability of other survey data that are deeper than UltraVISTA. Specifically, we employed the K -selected FIRES (Labbé et al. 2003; Förster Schreiber et al. 2006) and FIREWORKS (Wuyts et al. 2008) catalogs, already used in Marchesini et al. (2009, 2010) and the H_{160} -selected catalogs over the Hubble Ultra-Deep Field (HUDF) used in Marchesini et al. (2012). The FIRES-HDFS, FIRES-MS1054, FIREWORKS, and HUDF reach limiting magnitudes of $K_{s,\text{tot}} = 25.6, 24.1, 23.7$, and 25.6, respectively. The M_{star} values in these catalogs have been calculated using the same SED modeling assumptions as in the UltraVISTA catalog.

Briefly, to estimate the redshift-dependent stellar mass-completeness limit of the UltraVISTA sample at $K_{s,\text{tot}} = 23.4$, we first selected galaxies belonging to the available deeper samples. We then scaled their fluxes and M_{star} values to match the K -band completeness limit of the UltraVISTA sample. The upper envelope of points in ($M_{\text{star,scaled}}$ – z) space, encompassing 100% of the points, represents the most massive galaxies at $K_s = 23.4$ and so provides a redshift-dependent M_{star} completeness limit for the UltraVISTA sample. We refer the reader to Marchesini et al. (2009) for a more detailed description of this method. In Figure 2, we show this empirically derived 100% mass-completeness limit as a purple curve. Also, for reference we show the mass-completeness limit for a simple stellar population (SSP) formed at $z = 10$, which is extreme but indicative of a maximally old population.

Figure 2 shows that for galaxies at $z < 1.5$ and $K_{s,\text{tot}} \sim 23.4$, the most extreme mass-to-light (M/L) ratios are less extreme than for a SSP. Around $z = 1.5$, the SSP curve and the empirical 100% completeness curve cross each other, which implies that there exist galaxies that have larger M/L ratios than a SSP. Such galaxies are typically galaxies with intermediate-to-old ages (for their redshift) with up to several magnitudes of dust extinction. More detailed SED modeling for galaxies with spectroscopic redshifts shows that these dusty and old galaxies

are not uncommon among the massive galaxy population at $z > 1.5$ (see, e.g., Kriek et al. 2006, 2008; Muzzin et al. 2009a).

As Figure 2 shows, the empirically derived 100% mass-completeness limits are high due to the old and dusty population. Adopting the empirical 100% completeness limit for the SMFs therefore requires the exclusion of 57% of the magnitude-limited sample.

The 100% completeness limit is set by most extreme M/L ratio at any given redshift, regardless of the frequency of its occurrence. In principle, if only a small fraction of objects have these extreme M/L ratios, then adopting the 100% mass-completeness limit is an inefficient use of the data. In order to try to make better use of the dataset, we also derived 95% mass-completeness limits for the sample and this limit is plotted in Figure 2.

At all redshifts, the 95% mass-completeness limits are 0.2–0.3 dex lower, showing that it is only a small fraction of the overall population of galaxies that have extreme M/L ratios. If we adopt the 100% mass-completeness limits, the resulting sample of galaxies is 67,942. Adopting the 95% mass-completeness limits increases the sample by a factor of 1.4 to 95,675 galaxies. Given this substantial increase in statistics, and the advantage gained by probing further down the SMFs at higher redshift, we have adopted the 95% mass-completeness limits for the SMFs, but correct the lowest mass bin in each SMF by 5% in order to account for this.

3.3. Separation of Quiescent and Star-forming Galaxies

It is well known that the overall galaxy population is bimodal in the distribution of colors and SFRs (e.g., Kauffmann et al. 2003; Hogg et al. 2004; Balogh et al. 2004; Blanton & Moustakas 2009) and that this bimodality persists out to high redshift (e.g., Bell et al. 2004; Taylor et al. 2009; Williams et al. 2009; Brammer et al. 2009, 2011). Given the bimodality, separating the evolution of the SMFs of star-forming and quiescent galaxies as a function of redshift is useful for understanding the relationship between the two populations.

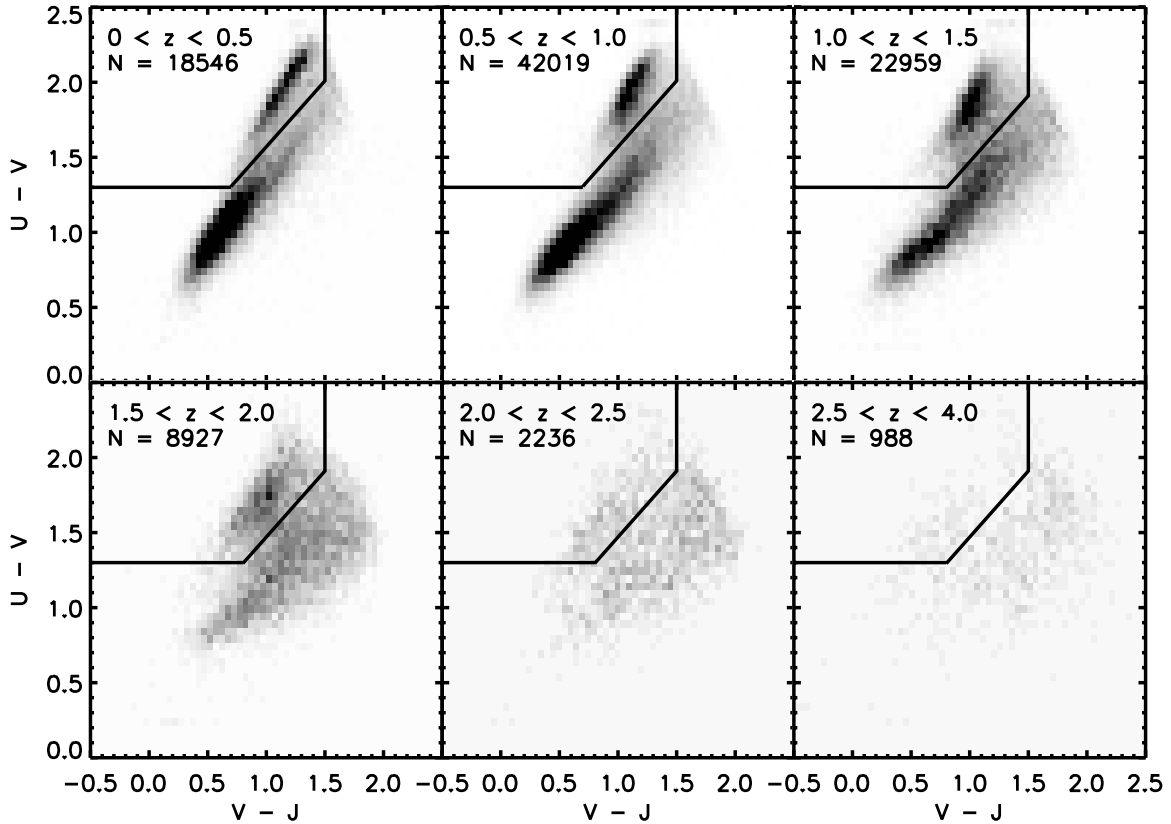


Figure 3. UVJ color–color diagram at various redshifts for galaxies more massive than the 95% mass completeness limits. The bimodality in the galaxy population is clearly visible up to $z = 2$. The cuts used to separate star forming from quiescent galaxies for the SMFs are shown as the solid lines.

In recent years, several methods have been developed to classify galaxies into these categories. In this analysis, we classify between the types using the rest-frame $U - V$ versus $V - J$ color–color diagram (hereafter, the UVJ diagram). UVJ classification has been used in many previous studies (e.g., Labb   et al. 2005; Wuyts et al. 2007; Williams et al. 2009; Brammer et al. 2011; Patel et al. 2012). These previous studies have shown that separation of star-forming and quiescent galaxies in this color–color space is well-correlated with separation using UV+IR determined specific star formation rates (SSFRs; e.g., Williams et al. 2009) and SED fitting-determined SSFRs (e.g., Williams et al. 2010) up to $z = 2.5$. Separation in this color space is also correlated with the detection and non-detection of galaxies at $24\,\mu\text{m}$, down to implied SFRs of $\sim 40\,M_{\odot}\,\text{yr}^{-1}$ at $z \sim 2$ (Wuyts et al. 2007; Brammer et al. 2011). We choose to separate galaxies based on a rest-frame color cut as opposed to a cut in a derived quantity such as SSFR because rest-frame colors can be calculated in a straightforward way for each galaxy in the sample. UV+IR SFRs can only be calculated for the most strongly star-forming galaxies at high redshift due to the limited depth of the $24\,\mu\text{m}$ data.

In Figure 3, we plot the $U - V$ versus $V - J$ diagram for galaxies more massive than the 95% mass-completeness limits in several redshift bins. The galaxy bimodality is clearly visible in the UVJ diagram up to $z = 2$, but thereafter becomes less pronounced at the M_{\star} completeness limits probed by the K_s -selected UltraVISTA catalog.

To distinguish between star-forming and quiescent galaxies, we use box regions in the UVJ diagram that are similar, although not identical, to those defined in Williams et al. (2009), Whitaker et al. (2011), and Brammer et al. (2011). These regions are

plotted as the solid lines in Figure 3. Quiescent galaxies are defined as

$$U - V > 1.3, V - J < 1.5, \text{ (all redshifts)} \quad (1)$$

$$U - V > (V - J) \times 0.88 + 0.69, \text{ (}0.0 < z < 1.0\text{)} \quad (2)$$

$$U - V > (V - J) \times 0.88 + 0.59, \text{ (}1.0 < z < 4.0\text{)}. \quad (3)$$

We note that these boxes are chosen arbitrarily, with the main criteria being that they lie roughly between the two modes of the population seen in Figure 3. They were originally defined by Williams et al. (2009), who defined them in such a way as to maximize the difference in SSFRs between the regions; however, our rest-frame color distribution is slightly different from that of Williams et al. (2009), which is the reason that we have adjusted the box locations. In Appendix B, we explore the effect on the SMFs of moving the location of the boxes in UVJ space. In general, we find that changing the UVJ box has little effect on the high-mass end of the quiescent SMF and the low-mass end of the star-forming SMF because those galaxies are dominated by very red and very blue galaxies, respectively. It does have a large effect on the SMF for intermediate mass galaxies, which is not unexpected given that these are typically the transition population at most redshifts.

3.4. Stellar Mass Function Construction and Fitting

With well-defined mass-completeness limits as a function of redshift and criteria for separating star-forming and quiescent galaxies, SMFs can now be computed. We employ two methods

to determine the SMFs: the $1/V_{\max}$ method and a maximum-likelihood method. These methods have different strengths and weaknesses. The $1/V_{\max}$ method has the advantage that it does not assume a parametric form of the SMF, allowing a direct visualization of the data; however, it is a fully normalized solution and is susceptible to the effects of clustering. Conversely, the maximum-likelihood method has the advantage that it is not affected by density inhomogeneities (e.g., Efstathiou et al. 1988); however, it does assume a functional form for the fit.

3.4.1. The $1/V_{\max}$ Method

To measure the SMFs for the sample, we have applied an extended version of the $1/V_{\max}$ algorithm (Schmidt 1968) as defined in Avni & Bahcall (1980). The method has been used to determine the rest-frame optical luminosity functions (LFs) and SMFs by Marchesini et al. (2007, 2009, 2010, 2012) and we refer the reader to those papers for a detailed description of the method.

In brief, for each M_{\star} , we determine the maximum volume within which an object of that M_{\star} could be detected. This volume is determined as a function of M_{\star} using the maximum redshift that the survey is complete to for objects with that M_{\star} . The SMF is then calculated by counting galaxies in bins of M_{\star} and correcting those bins by $1/V_{\max}$. Poisson error bars are determined for each bin using the prescription of Gehrels (1986), which is valid for small number statistics.

3.4.2. The Maximum-likelihood Method

The SMFs are also determined using the maximum-likelihood method outlined by Sandage et al. (1979). For this method, it is assumed that the number density of galaxies ($\Phi(M_{\star})$) is described by a Schechter (1976) function of the form

$$\Phi(M) = (\ln 10)\Phi^*[10^{(M-M^*)(1+\alpha)}] \times \exp[-10^{(M-M^*)}], \quad (4)$$

where $M = \log(M_{\star}/M_{\odot})$, α is the low-mass-end slope, $M^* = \log(M_{\star}^*/M_{\odot})$, where M_{\star}^* is the characteristic mass, and Φ^* is the normalization. For each possible combination of α and M_{\star}^* , the likelihood that each galaxy would be found in the survey is calculated. The best-fit solution for α and M_{\star}^* in each redshift bin is obtained by maximizing the combined likelihoods of all galaxies (Λ) with respect to these parameters. Φ^* is determined by requiring that the total number of observed galaxies is reproduced. The errors in Φ^* are then determined from the minimum and maximum values of Φ^* allowed by the confidence contours in the α versus M_{\star}^* plane. Further details of the fitting process can be found in Marchesini et al. (2007, 2009).

3.4.3. The Low-mass-end Slope α

The SMFs are computed over a large redshift range and, as was shown in Figure 2, the limiting 95% completeness limit in M_{\star} is a strong function of redshift. The SMFs reach ~ 1.5 dex deeper than M_{\star}^* at $z < 0.5$, but only to $\sim M_{\star}^*$ itself at $z = 3.5$. This means that α is well constrained at $z \leq 2$ but is poorly constrained at $z \geq 2$. Given the well-known correlation between α and M_{\star}^* , it is important to be aware that the true uncertainties in quantities such as M_{\star}^* or the SMD can be systematically larger than the random uncertainties due to the data not reaching a mass limit sufficiently low to constrain α . In order to better quantify the uncertainties in all parameters, we have performed in all redshift ranges a Schechter function fit both with α as a free parameter and fixing it to a known value.

In the fits with α held fixed, we have chosen values of $\alpha = -1.2, -0.4$, and -1.3 for the total, quiescent, and star-forming populations, respectively. As discussed in Section 4, these values are similar to those derived at $z < 1$ when α is fit as a free parameter. They are also consistent with values at $z > 1$ derived from studies that probe the low-mass end better than UltraVISTA (e.g., Fontana et al. 2006; Pérez-González et al. 2008; Marchesini et al. 2009; Stark et al. 2009; Lee et al. 2012).

In addition to fits with α fixed and free, we have also performed fits to a “double” Schechter function. Several recent studies have shown that at low redshift, the low-mass end of the SMF ($\log(M_{\star}/M_{\odot}) < 9.5$) is better described by the sum of two Schechter functions with identical M_{\star}^* , but different Φ^* and α (e.g., Li & White 2009; Baldry et al. 2012). The UltraVISTA SMFs reach the limiting M_{\star} where a clear departure from a single Schechter function fit is seen at $z < 1$. Accordingly, the SMFs in that redshift range, fits are also performed with a double Schechter function.

3.4.4. Determination of Uncertainties in the SMFs

In addition to the Poisson uncertainties, there are several other sources of uncertainty in the construction of SMFs that need to be taken into account. The largest are caused by the fact that M_{\star} itself is not an observable quantity, but is derived from observables (i.e., multiwavelength photometry) using a set of models. The effect of photometric uncertainties on the derived values of z_{phot} and M_{\star} is a non-trivial function of color, magnitude, and redshift caused by a range of data depths in various bands within the survey.

In order to calculate uncertainties in the SMFs due to photometric uncertainties, we perform 100 Monte Carlo (MC) realizations of the catalog. Within each realization, the photometry in the catalog is perturbed using the measured photometric uncertainties. New z_{phot} and M_{\star} values are calculated for each galaxy using the perturbed catalog. The 100 MC catalogs are then used to recalculate the SMFs and the range of values gives an empirical estimate of the uncertainties in the SMFs due to uncertainties in M_{\star} and z_{phot} that propagate from the photometric uncertainties.

In addition to these z_{phot} and M_{\star} uncertainties, the uncertainty from cosmic variance is also included using the prescriptions of Moster et al. (2011). In Figure 4, we plot the uncertainty in the abundance of galaxies with $\log(M_{\star}/M_{\odot}) = 11.0$ due to cosmic variance as a function of redshift. Cosmic variance is most pronounced at the high-mass end where galaxies are more clustered and at low redshift, where the survey volume is smallest. Also plotted in Figure 4 are the cosmic variance uncertainties from other NIR surveys such as FIREWORKS (Wuyts et al. 2008), MUYSIC (Quadri et al. 2007; Marchesini et al. 2009), NMBS (Whitaker et al. 2011), and the UDS (Williams et al. 2009). These surveys cover areas that are factors of ~ 50 , 16, 4, and 2 smaller than UltraVISTA, respectively. Figure 4 shows that the larger area of UltraVISTA offers a factor of 1.5 improvement in the uncertainties in cosmic variance compared with even the best previous surveys; over the full redshift range, the uncertainty from cosmic variance is $\sim 8\%-15\%$ at $\log(M_{\star}/M_{\odot}) = 11.0$.

The total uncertainties in the determination of the SMFs are derived as follows. For the $1/V_{\max}$ method, the total 1σ random error in each mass bin is the quadrature sum of the Poisson error, the error from photometric uncertainties as derived using the MC realizations, and the error due to cosmic variance. For the maximum-likelihood method, the total 1σ random errors

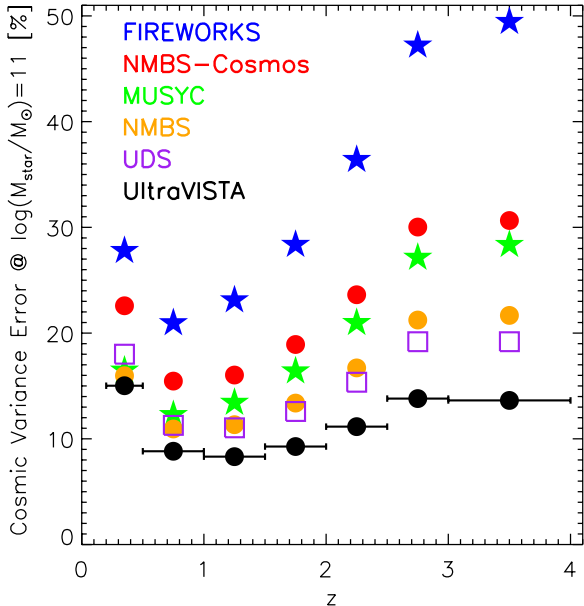


Figure 4. Uncertainty in the number density of galaxies with $\log(M_{\text{star}}/M_{\odot}) = 11.0$ due to cosmic variance as a function of redshift calculated using the prescription of Moster et al. (2011). Other surveys with smaller areas but also more independent sight lines are shown for comparison (see the text for details). The uncertainties in UltraVISTA due to cosmic variance are $\sim 8\%-15\%$ at $\log(M_{\text{star}}/M_{\odot}) = 11.0$ over the full redshift range.

(A color version of this figure is available in the online journal.)

of the Schechter function parameters α , M_{star}^* , and Φ^* are the quadrature sum of the errors from the maximum-likelihood analysis, the errors from photometric uncertainties as derived using the MC realizations, and the error due to cosmic variance (affecting only the normalization Φ^*).

4. THE STELLAR MASS FUNCTIONS, MASS DENSITIES, AND NUMBER DENSITIES TO $z = 4$

4.1. The Stellar Mass Functions

In Figure 5, we plot the best-fit maximum-likelihood SMFs for the star-forming, quiescent, and combined populations of galaxies. Figure 5 illustrates the redshift evolution of the SMFs of the individual populations, which we discuss in detail in Section 5. To better illustrate the relative contribution of both star-forming and quiescent galaxies to the combined SMF, we plot in Figure 6 the SMFs derived using the $1/V_{\text{max}}$ method (points), as well as the fits from the maximum-likelihood method (filled regions) in the same redshift bins. The SMFs of the combined population are plotted in the top panels, and the SMFs of the star-forming and quiescent populations are plotted in the middle panels. Within each of the higher redshift bins, the SMFs from the lowest redshift bin ($0.2 < z < 0.5$) are shown as the dotted line as a fiducial to demonstrate the relative evolution of the SMFs. The fraction of quiescent galaxies as a function of M_{star} is shown in the bottom panels and the best-fit Schechter function parameters for these redshift ranges are listed in Table 1.

For reference, in the lowest redshift panel ($0.2 < z < 0.5$) of Figure 6 we plot the SMFs at $z \sim 0.1$ for the total population from the studies of Cole et al. (2001), Bell et al. (2003), and Baldry et al. (2012). Plotted in the middle panel of the lowest redshift bin are the SMFs of star-forming and quiescent galaxies from Bell et al. (2003) and Baldry et al. (2012). Qualitatively, these are similar to our measurements, although we note that

the selection of star-forming and quiescent galaxies is done differently than the UVJ selection in UltraVISTA.

4.2. The Stellar Mass Density and Number Density

In the left panel of Figure 7, we plot the integrated SMD of all galaxies as a function of redshift. For consistency with other studies in the literature, the SMDs have been calculated by integrating the maximum-likelihood Schechter function fits down to a limit of $\log(M_{\text{star}}/M_{\odot}) = 8.0$ at each redshift. We perform this integration using the full maximum-likelihood fit, even though at $z > 2$ α is not well constrained. In order to account for possible systematic errors caused by an underestimate of α due to the limited data depth, we also include at all redshifts the uncertainties from the maximum-likelihood fits with $\alpha = -1.2$. Therefore, the quoted uncertainties in Figure 7, and all subsequent figures that use integration of the SMFs, span the full range of uncertainties for both the α -free and α -fixed SMFs.

Overplotted in Figure 7 are measurements of the SMD at various redshifts from previous studies by Cole et al. (2001, C01), Bell et al. (2003, B03), Drory et al. (2005, D05), Rudnick et al. (2006, R06), Fontana et al. (2006, F06), Elsner et al. (2008, E08), Pérez-González et al. (2008, P08), Marchesini et al. (2009, M09), Kajisawa et al. (2009, K09), Drory et al. (2009, D09), Marchesini et al. (2010, M10), Ilbert et al. (2010, I10), Mortlock et al. (2011, M11), Baldry et al. (2012, B12), Bielby et al. (2012, Bi12), Santini et al. (2012, S12), and Moustakas et al. (2013, M13). The substantially larger volume covered by UltraVISTA allows for an impressive improvement in the uncertainties in the evolution of the SMDs. Within the uncertainties, the majority of previous measurements agree reasonably well with the UltraVISTA measurements, particularly at $z < 2$. At $z > 2$, there is less agreement with previous datasets; the UltraVISTA SMDs are lower than some previous works such as Elsner et al. (2008), Pérez-González et al. (2008), and Santini et al. (2012). The disagreement with Elsner et al. (2008) and Pérez-González et al. (2008) is because those studies measure a larger Φ^* than UltraVISTA. The discrepancy with Santini et al. (2012) is primarily because they measure a steep value of α at $z > 2$.

SMDs and their uncertainties for star-forming and quiescent galaxies have also been computed using the same integration method as for the total SMD. These are plotted in the left panel of Figure 8 as a function of redshift. In general, it is clear that at $z < 3.5$, the SMD of quiescent galaxies grows faster than that of star-forming galaxies. We explore the implications of this further in Section 5. All SMDs are listed in Table 2.

In the right panel of Figure 7, we plot the evolution of the integrated number densities of galaxies calculated using the same Schechter function fits. The number densities are determined down to limiting masses of $\log(M_{\text{star}}/M_{\odot}) = 11.5$, 11.0, 10.0, and 8.0, and these points are labeled in the figure. The number densities measured from the NMBS survey (Brammer et al. 2011) for mass limits of $\log(M_{\text{star}}/M_{\odot}) = 11.0$ and 10.0 are plotted as black points. These points were measured using a catalog constructed in a similar way as the UltraVISTA catalog and agree well with the number densities in UltraVISTA. Also shown in Figure 7 are the integrated number densities at $z < 1$ calculated from the PRIMUS survey (Moustakas et al. 2013), which covers an area $\sim 3\times$ larger than UltraVISTA. These are also consistent with the UltraVISTA measurements. Similar integrated number densities for both the star-forming and quiescent populations are shown in the right panel of Figure 8 and the values are listed in Table 2.

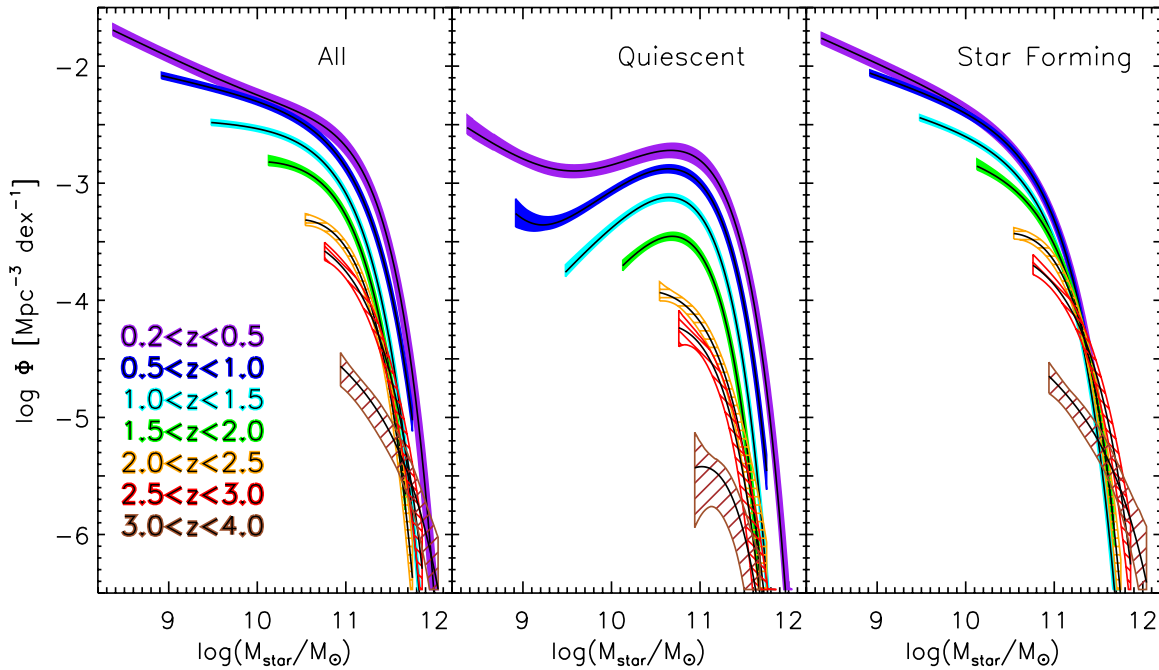


Figure 5. Stellar mass functions of all galaxies, quiescent galaxies, and star-forming galaxies in different redshift intervals. The shaded/hatched regions represent the total 1σ uncertainties of the maximum-likelihood analysis, including cosmic variance and the errors from photometric uncertainties derived using the MC realizations. The normalization of the SMF of quiescent galaxies evolves rapidly with redshift, whereas the normalization for star-forming galaxies evolves relatively slowly. In particular, there is almost no change at the high-mass end of the star-forming SMF, whereas there is clear growth at the high-mass end of the quiescent population. There is also evidence for evolution of the low-mass-end slope for quiescent galaxies. At low redshift, a double Schechter function fit is required to reproduce the total SMF.

(A color version of this figure is available in the online journal.)

5. DISCUSSION

5.1. The Combined Population

In Figure 9, we plot the evolution of the Schechter parameters M_{star}^* , Φ^* , and α as a function of redshift for the combined population of both star-forming and quiescent galaxies. All points plotted are from the single Schechter function fits except for the $0.2 < z < 0.5$ bin, where we have plotted the M_{star}^* and combined Φ^* 's of the double Schechter function fits. We do not plot α at $z > 2$ in Figure 9 because the limiting mass of the data at these redshifts is too high to provide constraints. The lack of constraints, combined with the correlation between M_{star}^* and α , means that the uncertainties in α at $z > 2$ are likely to be underestimated. Also plotted in Figure 9 are the best-fit Schechter parameters from the low-redshift SMFs from Cole et al. (2001) and Bell et al. (2003) and the high-redshift rest-frame-optical-selected SMFs from Pérez-González et al. (2008), Marchesini et al. (2009), Marchesini et al. (2010), and Caputi et al. (2011).

A comparison of the parameters in our lowest redshift bin ($0.2 < z < 0.5$) with those parameters from Cole et al. (2001) and Bell et al. (2003) shows good agreement for both M_{star} and Φ^* . There is some disagreement in α , with our data having a steeper low-mass-end slope than the local SMFs. It is unclear why this is, as the UltraVISTA data reach a comparable depth in M_{star} as local studies. Part of the discrepancy may be because Cole et al. (2001) and Bell et al. (2003) fit a single Schechter function when a double function is required. If we compare our double Schechter function fits ($\alpha_1 = -0.53^{+0.16}_{-0.28}$, $\alpha_2 = -1.37^{+0.01}_{-0.06}$) with those derived from Baldry et al. (2012) ($\alpha_1 = -0.35 \pm 0.18$, $\alpha_2 = -1.47 \pm 0.05$), we find good agreement.

Figure 9 also shows that there is good agreement between our SMFs and previous high-redshift SMFs in the literature. There

is a significant improvement in the uncertainties in the SMFs derived from the UltraVISTA catalog, mostly due to the fact it covers an area that is a factor of 8.8 and 11.4 larger than the areas used in the Pérez-González et al. (2008) and Marchesini et al. (2009) studies, respectively. Figure 9 confirms the results of those previous works and shows that within the substantially smaller uncertainties, there is still no significant evolution in M_{star}^* out to $z \sim 3.0$. This lack of evolution implies that whatever process causes the exponential tail of the Schechter function does so in a consistent way over much of cosmic time. At $z > 3.5$, we find some evidence for a change in M_{star}^* ; however, given the lack of constraints on α at this redshift and the correlation between M_{star}^* and α , the uncertainties are still large.

Although there is no significant evolution in M_{star}^* , there is a substantial evolution in Φ^* from $z = 3.5$ to $z = 0.0$. If we compare with the Φ^* at $z = 0$ from Cole et al. (2001), we find that it evolves by $2.58^{+1.01}_{-0.37}$ dex between $z \sim 3.5$ and $z \sim 0.0$. As Figure 9 shows, this evolution is stronger than the values of 1.22 ± 0.43 , $1.76^{+0.40}_{-0.82}$, $1.92^{+0.39}_{-0.36}$, and $1.89^{+0.14}_{-0.19}$ dex measured previously by Pérez-González et al. (2008), Marchesini et al. (2009), Marchesini et al. (2010), and Caputi et al. (2011), respectively.

Interestingly, it appears that there is a statistically significant evolution in α up to $z = 2$, the redshift where the data are deep enough that there are still reasonable constraints on α . A flattening of the slope with redshift was also seen in the SMFs of Marchesini et al. (2009), which probe to slightly lower M_{star} . Such a flattening in the combined population is a natural consequence of the fact that there appears to be little evolution in the α of the star-forming population, but a flattening in α for the quiescent population with increasing redshift (e.g., Figure 5; see Section 5.2). UV-selected samples suggest a steep α at

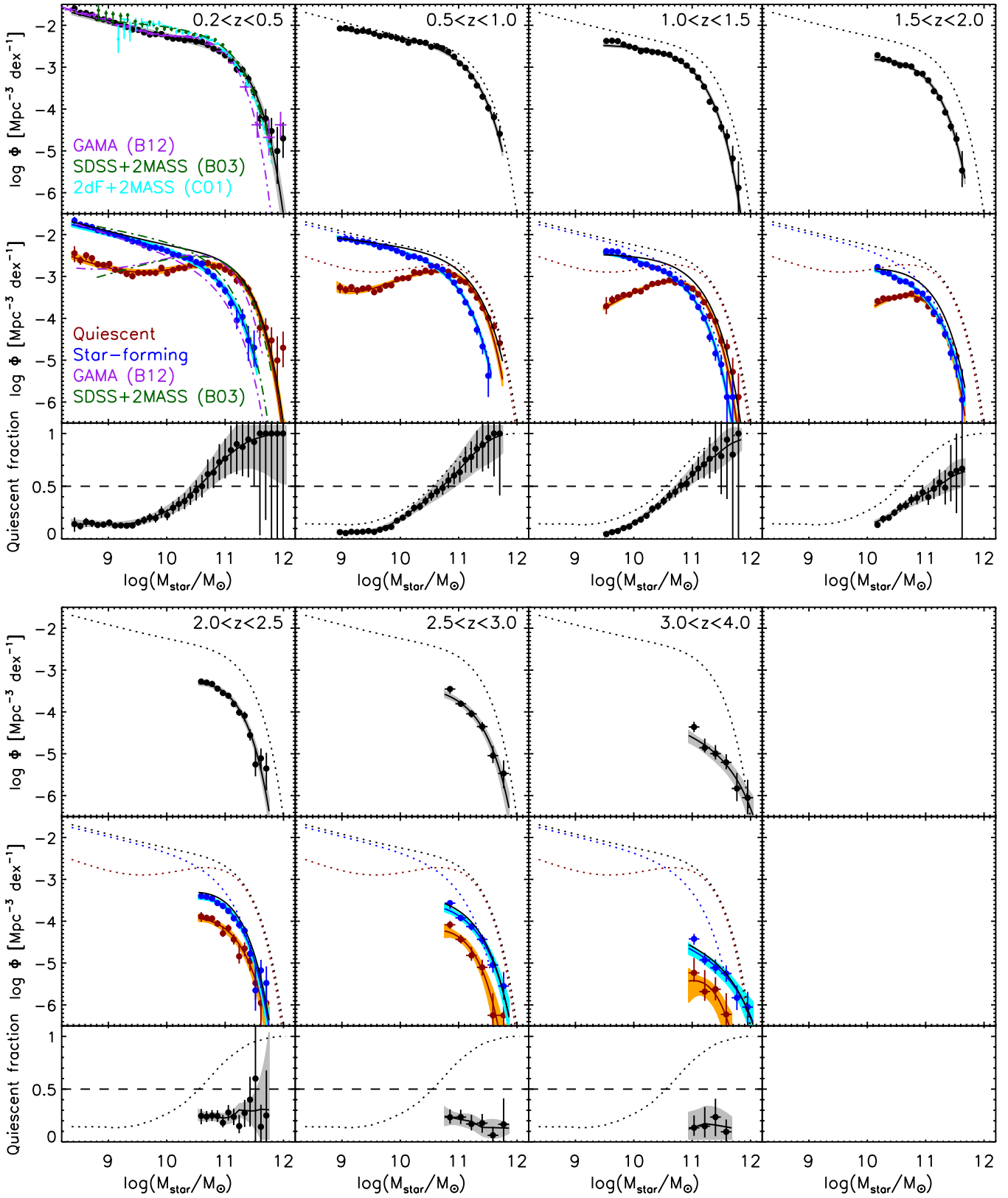


Figure 6. Top panels: the SMFs of all galaxies in different redshift bins from $0.2 < z < 4.0$. The black points represent the SMFs determined using the $1/V_{\max}$ method and the black solid curves are the SMFs determined using the maximum-likelihood method. The gray shaded regions represent the total 1σ uncertainties of the maximum-likelihood analysis, including cosmic variance and the errors from photometric uncertainties as derived from the MC simulations. Overplotted in the $0.2 < z < 0.5$ bin are the SMFs from Cole et al. (2001), Bell et al. (2003), and Baldry et al. (2012). In the remaining redshift bins, the dotted curve is the total SMF from UltraVISTA in the $0.2 < z < 0.5$ bin. Middle panels: SMFs as in the top panels, but for the quiescent galaxies (red points, red solid curves) and star-forming galaxies (blue points, blue solid curves). The orange and cyan shaded regions represent the total 1σ uncertainties of the maximum-likelihood analysis for quiescent and star-forming galaxies, respectively. Bottom panels: fraction of quiescent galaxies as a function of M_{\star} .

(A color version of this figure is available in the online journal.)

Table 1
Best-fit Schechter Function Parameters for the SMFs

Redshift	Sample	Number	$\log M_{\star}^{\text{lim}}$ (M_{\odot})	$\log M_{\star}^{\star}$ (M_{\odot})	Φ^{\star} (10^{-4} Mpc^{-3})	α	Φ_2^{\star} (10^{-4} Mpc^{-3})	α_2
$0.2 \leq z < 0.5$	All	18546	8.37	$11.22^{+0.03}_{-0.03}(0.03)$	$12.16^{+0.52}_{-0.50}(^{+1.75}_{-1.55})$	$-1.29 \pm 0.01(0.01)$
$0.2 \leq z < 0.5$	All	18546	8.37	$11.06 \pm 0.01(0.01)$	$19.02 \pm 0.14(2.31)$	-1.2
$0.2 \leq z < 0.5$	All	18546	8.37	$10.97 \pm 0.06(0.06)$	$16.27^{+3.12}_{-1.39}(^{+3.88}_{-2.41})$	$-0.53^{+0.16}_{-0.27}(^{+0.16}_{-0.28})$	$9.47^{+2.02}_{-3.64}(^{+2.32}_{-3.83})$	$-1.37^{+0.01}_{-0.06}(^{+0.01}_{-0.06})$
$0.2 \leq z < 0.5$	Quiescent	4364	8.37	$11.21 \pm 0.03(0.04)$	$10.09 \pm 0.54(^{+1.69}_{-1.33})$	$-0.92 \pm 0.02(^{+0.04}_{-0.02})$
$0.2 \leq z < 0.5$	Quiescent	4364	8.37	$10.75 \pm 0.01(0.01)$	$30.65 \pm 0.01(3.71)$	-0.4
$0.2 \leq z < 0.5$	Quiescent	4364	8.37	$10.92^{+0.06}_{-0.02}(^{+0.06}_{-0.02})$	$19.68^{+1.09}_{-1.73}(^{+2.64}_{-2.96})$	$-0.38^{+0.06}_{-0.11}(^{+0.06}_{-0.12})$	$0.58^{+0.26}_{-0.31}(^{+0.27}_{-0.32})$	$-1.52^{+0.06}_{-0.16}(^{+0.06}_{-0.16})$
$0.2 \leq z < 0.5$	Star-forming	14182	8.37	$10.81 \pm 0.03(0.03)$	$11.35^{+0.76}_{-0.67}(^{+1.60}_{-1.51})$	$-1.34 \pm 0.01(0.01)$
$0.2 \leq z < 0.5$	Star-forming	14182	8.37	$10.75 \pm 0.01(0.01)$	$13.58^{+0.15}_{-0.13}(^{+1.62}_{-1.59})$	-1.3
$0.5 \leq z < 1.0$	All	42019	8.92	$11.00^{+0.02}_{-0.01}(^{+0.02}_{-0.01})$	$16.25^{+0.28}_{-0.62}(^{+1.17}_{-1.28})$	$-1.17 \pm 0.01(0.01)$
$0.5 \leq z < 1.0$	All	42019	8.92	$11.04 \pm 0.01(0.01)$	$14.48 \pm 0.07(1.00)$	-1.2
$0.5 \leq z < 1.0$	Quiescent	9127	8.92	$10.87^{+0.02}_{-0.01}(^{+0.02}_{-0.01})$	$13.68^{+0.26}_{-0.36}(^{+1.09}_{-1.01})$	$-0.44 \pm 0.02(^{+0.04}_{-0.02})$
$0.5 \leq z < 1.0$	Quiescent	9127	8.92	$10.84 \pm 0.01(0.02)$	$14.38 \pm 0.02(0.99)$	-0.4
$0.5 \leq z < 1.0$	Quiescent	9127	8.92	$10.84 \pm 0.02(0.03)$	$14.55^{+0.56}_{-0.42}(^{+1.21}_{-1.09})$	$-0.36^{+0.06}_{-0.03}(^{+0.06}_{-0.04})$	$0.005^{+0.021}_{-0.003}(^{+0.021}_{-0.004})$	$-2.32^{+0.40}_{-0.32}(^{+0.41}_{-0.38})$
$0.5 \leq z < 1.0$	Star-forming	32892	8.92	$10.78^{+0.01}_{-0.02}$	$12.71^{+0.51}_{-0.29}(^{+1.07}_{-0.91})$	$-1.26 \pm 0.01(^{+0.02}_{-0.01})$
$0.5 \leq z < 1.0$	Star-forming	32892	8.92	$10.82 \pm 0.01(0.02)$	$10.95^{+0.06}_{-0.08}(0.73)$	-1.3
$1.0 \leq z < 1.5$	All	22959	9.48	$10.87^{+0.02}_{-0.01}(^{+0.02}_{-0.01})$	$13.91^{+0.43}_{-0.59}(^{+1.05}_{-1.23})$	$-1.02 \pm 0.02(0.02)$
$1.0 \leq z < 1.5$	All	22959	9.48	$10.99 \pm 0.01(0.01)$	$9.30 \pm 0.06(0.66)$	-1.2
$1.0 \leq z < 1.5$	Quiescent	6455	9.48	$10.73 \pm 0.02(0.02)$	$8.81 \pm 0.19(0.63)$	$-0.17 \pm 0.04(^{+0.06}_{-0.04})$
$1.0 \leq z < 1.5$	Quiescent	6455	9.48	$10.83 \pm 0.01(0.02)$	$7.48 \pm 0.02(^{+0.51}_{-0.56})$	-0.4
$1.0 \leq z < 1.5$	Star-forming	16504	9.48	$10.76 \pm 0.02(0.02)$	$8.87^{+0.50}_{-0.54}(^{+0.79}_{-0.86})$	$-1.21 \pm 0.03(0.03)$
$1.0 \leq z < 1.5$	Star-forming	16504	9.48	$10.82 \pm 0.01(0.01)$	$7.20^{+0.06}_{-0.11}(0.49)$	-1.3
$1.5 \leq z < 2.0$	All	8927	10.03	$10.81 \pm 0.02(^{+0.02}_{-0.03})$	$10.13^{+0.58}_{-0.56}(^{+1.11}_{-1.02})$	$-0.86 \pm 0.06(^{+0.11}_{-0.06})$
$1.5 \leq z < 2.0$	All	8927	10.03	$10.96 \pm 0.01(^{+0.03}_{-0.01})$	$6.33^{+0.06}_{-0.11}(^{+0.53}_{-0.71})$	-1.2
$1.5 \leq z < 2.0$	Quiescent	2656	10.03	$10.67 \pm 0.03(0.04)$	$4.15^{+0.06}_{-0.08}(^{+0.35}_{-0.36})$	$0.03 \pm 0.11(0.12)$
$1.5 \leq z < 2.0$	Quiescent	2656	10.03	$10.80 \pm 0.01(0.02)$	$3.61^{+0.02}_{-0.04}(0.30)$	-0.4
$1.5 \leq z < 2.0$	Star-forming	6271	10.03	$10.85^{+0.02}_{-0.03}(^{+0.02}_{-0.04})$	$5.68^{+0.60}_{-0.40}(^{+0.89}_{-0.65})$	$-1.16^{+0.07}_{-0.05}(^{+0.14}_{-0.06})$
$1.5 \leq z < 2.0$	Star-forming	6271	10.03	$10.91 \pm 0.01(^{+0.04}_{-0.01})$	$4.49 \pm 0.09(^{+0.39}_{-0.60})$	-1.3
$2.0 \leq z < 2.5$	All	2236	10.54	$10.81 \pm 0.05(^{+0.06}_{-0.05})$	$4.79^{+0.28}_{-0.41}(^{+0.70}_{-0.76})$	$-0.55^{+0.16}_{-0.19}(^{+0.22}_{-0.24})$
$2.0 \leq z < 2.5$	All	2236	10.54	$11.00 \pm 0.02(0.02)$	$2.94^{+0.07}_{-0.11}(0.40)$	-1.2
$2.0 \leq z < 2.5$	Quiescent	528	10.54	$10.87 \pm 0.10(^{+0.11}_{-0.17})$	$1.02^{+0.17}_{-0.23}(^{+0.30}_{-0.27})$	$-0.71^{+0.37}_{-0.33}(^{+0.67}_{-0.39})$
$2.0 \leq z < 2.5$	Quiescent	528	10.54	$10.79 \pm 0.02(0.03)$	$1.14 \pm 0.05(0.18)$	-0.4
$2.0 \leq z < 2.5$	Star-forming	1708	10.54	$10.80 \pm 0.05(0.06)$	$3.72^{+0.25}_{-0.32}(^{+0.58}_{-0.66})$	$-0.53^{+0.22}_{-0.19}(^{+0.28}_{-0.24})$
$2.0 \leq z < 2.5$	Star-forming	1708	10.54	$11.03 \pm 0.02(^{+0.03}_{-0.02})$	$2.01^{+0.08}_{-0.10}(^{+0.28}_{-0.30})$	-1.3
$2.5 \leq z < 3.0$	All	814	10.76	$11.03^{+0.10}_{-0.09}(^{+0.12}_{-0.11})$	$1.93^{+0.43}_{-0.51}(^{+0.62}_{-0.68})$	$-1.01^{+0.37}_{-0.34}(^{+0.45}_{-0.41})$
$2.5 \leq z < 3.0$	All	814	10.76	$11.09 \pm 0.02(0.03)$	$1.66 \pm 0.10(0.34)$	-1.2
$2.5 \leq z < 3.0$	Quiescent	178	10.76	$10.80^{+0.23}_{-0.17}(^{+0.27}_{-0.21})$	$0.65^{+0.12}_{-0.24}(^{+0.18}_{-0.27})$	$-0.39^{+1.03}_{-0.95}(^{+1.18}_{-1.11})$
$2.5 \leq z < 3.0$	Quiescent	178	10.76	$10.81 \pm 0.04(0.05)$	$0.66^{+0.08}_{-0.07}(^{+0.17}_{-0.14})$	-0.4
$2.5 \leq z < 3.0$	Star-forming	636	10.76	$11.06^{+0.13}_{-0.10}(^{+0.14}_{-0.12})$	$1.39^{+0.35}_{-0.48}(^{+0.47}_{-0.57})$	$-1.03 \pm 0.39(0.47)$
$2.5 \leq z < 3.0$	Star-forming	636	10.76	$11.14 \pm 0.03(^{+0.05}_{-0.03})$	$1.09 \pm 0.09(^{+0.22}_{-0.26})$	-1.3
$3.0 \leq z < 4.0$	All	174	10.94	$11.49^{+0.36}_{-0.22}(^{+0.37}_{-0.28})$	$0.09^{+0.09}_{-0.07}(^{+0.15}_{-0.08})$	$-1.45^{+0.59}_{-0.54}(^{+0.70}_{-0.60})$
$3.0 \leq z < 4.0$	All	174	10.94	$11.40 \pm 0.06(0.08)$	$0.13 \pm 0.02(^{+0.08}_{-0.04})$	-1.2
$3.0 \leq z < 4.0$	Quiescent	28	10.94	$10.85^{+0.64}_{-0.32}(^{+0.76}_{-0.43})$	$0.04^{+0.03}_{-0.04}(^{+0.05}_{-0.04})$	$0.46^{+3.16}_{-2.41}(^{+3.30}_{-2.78})$
$3.0 \leq z < 4.0$	Quiescent	28	10.94	$11.00 \pm 0.10(^{+0.14}_{-0.11})$	$0.05^{+0.02}_{-0.01}(^{+0.05}_{-0.02})$	-0.4
$3.0 \leq z < 4.0$	Star-forming	146	10.94	$11.56^{+0.44}_{-0.25}(^{+0.45}_{-0.33})$	$0.06^{+0.08}_{-0.05}(^{+0.12}_{-0.05})$	$-1.51^{+0.61}_{-0.55}(^{+0.77}_{-0.62})$
$3.0 \leq z < 4.0$	Star-forming	146	10.94	$11.47 \pm 0.07(^{+0.08}_{-0.10})$	$0.08 \pm 0.02(^{+0.05}_{-0.03})$	-1.3

Note. The listed errors are the 1σ Poisson errors, whereas the values in parentheses list the total 1σ errors, including Poisson uncertainties, the uncertainties from photometric redshift random errors, and cosmic variance.

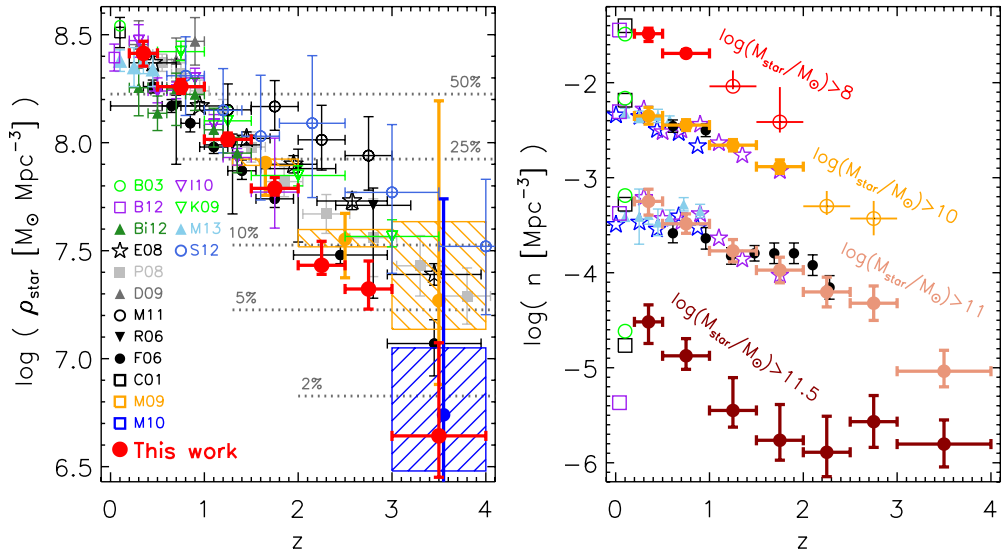


Figure 7. Left panel: the evolution of the stellar mass density of galaxies from $z = 4$ to $z = 0$ down to a limit of $\log(M_{\text{star}}/M_{\odot}) = 8.0$. The UltraVISTA measurements are shown in red with error bars representing total 1σ random errors inclusive of cosmic variance and the errors from photometric uncertainties as derived using the MC simulations. Other measurements from the literature are shown (see the text for the definitions of the references) and agree well with the UltraVISTA measurements within the uncertainties. Right panel: the evolution of the number density of galaxies above a fixed mass limit from UltraVISTA. Open circles denote extrapolations of the Schechter function beyond the data. The black points, light blue triangles, purple stars, and blue stars are NMBS (Brammer et al. 2011), PRIMUS (Moustakas et al. 2013), S-COSMOS (Ilbert et al. 2010), and zCOSMOS (Pozzetti et al. 2010) data, respectively, and all agree well with the UltraVISTA measurements.

(A color version of this figure is available in the online journal.)

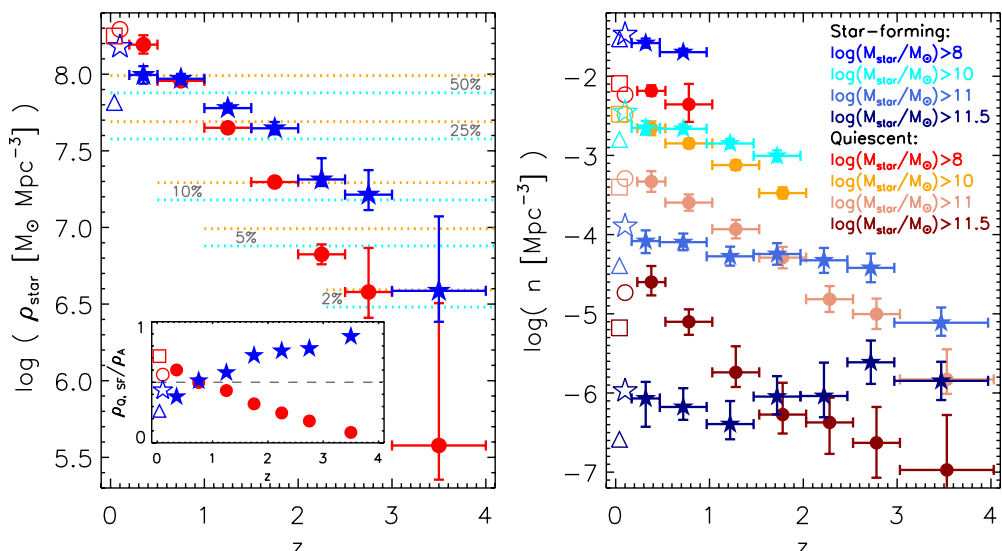


Figure 8. Left panel: the evolution of the stellar mass density of star-forming (blue) and quiescent (red) galaxies as a function of redshift with error bars representing total 1σ random errors inclusive of cosmic variance and the errors from photometric uncertainties as derived using the MC simulations. At low redshift the measurements from Bell et al. (2003; circles and stars) and Baldry et al. (2012; squares and triangles) are shown. The mass density in quiescent galaxies evolves faster than the mass density in star-forming galaxies, particularly at high redshift. Although they dominate the high-mass end of the mass function at $z < 2.5$, quiescent galaxies do not dominate the overall mass density of the universe until $z < 0.75$ due to a much shallower low-mass-end slope. Right panel: evolution of the number densities of star-forming and quiescent galaxies at a fixed mass limit as a function of redshift.

(A color version of this figure is available in the online journal.)

high redshift (e.g., Reddy & Steidel 2009; Stark et al. 2009; González et al. 2011; Lee et al. 2012), which, taken at face value, disagrees with the flattening of the slope observed for the K_s -selected SMF. As we show in Section 5.3, UV selection misses a fraction of the massive galaxy population due to their quiescence and/or dustiness, so α may be overestimated for the combined population.

Recently, Santini et al. (2012) measured the faint-end slope using ultra-deep HAWK-I K_s data, which provides a better comparison with the UltraVISTA SMFs than UV-selected SMFs.

They also find a steep faint-end slope ($\alpha = -1.84 \pm 0.06$) at $z \sim 2$, which, taken at face value, does not agree well with our measurement. Of course, α and M_{star}^* are correlated and Santini et al. (2012) cover an area that is two orders of magnitude smaller than that of UltraVISTA and therefore they have poor constraints on M_{star}^* . At $z \sim 2$, they find a value of $\log(M_{\text{star}}^*/M_{\odot}) = 11.82 \pm 0.28$, which is almost an order of magnitude larger than the UltraVISTA value of $\log(M_{\text{star}}^*/M_{\odot}) = 10.81^{+0.06}_{-0.05}$. This makes it clear that in order to simultaneously fit the Santini et al. (2012) measurements and

Table 2
Number and Stellar Mass Densities

Redshift	Density	$\log\left(\frac{M_{\text{star}}}{M_{\odot}}\right) > 8$	$\log\left(\frac{M_{\text{star}}}{M_{\odot}}\right) > 9$	$\log\left(\frac{M_{\text{star}}}{M_{\odot}}\right) > 10$	$\log\left(\frac{M_{\text{star}}}{M_{\odot}}\right) > 11$	$\log\left(\frac{M_{\text{star}}}{M_{\odot}}\right) > 11.5$
0.2 $\leq z < 0.5$	$\log(\eta_A)$	-1.49 ± 0.06	-1.89 ± 0.07	-2.35 ± 0.09	-3.25 ± 0.13	$-4.52^{+0.18}_{-0.23}$
	$\log(\eta_Q)$	$-2.19^{+0.07}_{-0.06}$	-2.45 ± 0.07	-2.66 ± 0.09	-3.33 ± 0.13	$-4.60^{+0.20}_{-0.17}$
	$\log(\eta_{SF})$	-1.58 ± 0.06	-2.03 ± 0.07	-2.65 ± 0.09	$-4.08^{+0.13}_{-0.15}$	$-6.07^{+0.21}_{-0.36}$
	$\log(\rho_A)$	8.41 ± 0.06	8.40 ± 0.07	8.35 ± 0.09	$7.98^{+0.13}_{-0.14}$	$7.08^{+0.18}_{-0.23}$
	$\log(\rho_Q)$	8.19 ± 0.06	8.19 ± 0.07	8.18 ± 0.09	7.91 ± 0.13	$7.00^{+0.21}_{-0.17}$
	$\log(\rho_{SF})$	7.99 ± 0.06	7.97 ± 0.07	7.85 ± 0.09	$7.08^{+0.14}_{-0.16}$	$5.50^{+0.21}_{-0.35}$
0.5 $\leq z < 1.0$	$\log(\eta_A)$	-1.69 ± 0.04	-2.00 ± 0.04	-2.45 ± 0.06	-3.49 ± 0.11	$-4.88^{+0.18}_{-0.14}$
	$\log(\eta_Q)$	$-2.36^{+0.26}_{-0.22}$	-2.70 ± 0.04	-2.85 ± 0.06	-3.60 ± 0.10	$-5.10^{+0.16}_{-0.17}$
	$\log(\eta_{SF})$	$-1.70^{+0.04}_{-0.03}$	-2.09 ± 0.04	-2.66 ± 0.06	$-4.10^{+0.11}_{-0.10}$	$-6.18^{+0.24}_{-0.16}$
	$\log(\rho_A)$	8.26 ± 0.03	8.25 ± 0.04	8.19 ± 0.06	$7.73^{+0.11}_{-0.10}$	$6.72^{+0.19}_{-0.14}$
	$\log(\rho_Q)$	7.96 ± 0.03	7.96 ± 0.04	7.94 ± 0.06	7.61 ± 0.10	$6.48^{+0.16}_{-0.17}$
	$\log(\rho_{SF})$	7.97 ± 0.03	7.95 ± 0.04	7.84 ± 0.06	7.06 ± 0.11	$5.39^{+0.24}_{-0.16}$
1.0 $\leq z < 1.5$	$\log(\eta_A)$	$-2.04^{+0.17}_{-0.03}$	$-2.26^{+0.07}_{-0.04}$	-2.66 ± 0.06	-3.77 ± 0.12	$-5.45^{+0.35}_{-0.18}$
	$\log(\eta_Q)$	$-3.01^{+0.05}_{-0.03}$	$-3.01^{+0.05}_{-0.04}$	-3.12 ± 0.06	-3.93 ± 0.12	$-5.74^{+0.33}_{-0.19}$
	$\log(\eta_{SF})$	$-1.94^{+0.10}_{-0.04}$	$-2.30^{+0.05}_{-0.04}$	-2.85 ± 0.06	-4.27 ± 0.12	$-6.39^{+0.29}_{-0.19}$
	$\log(\rho_A)$	8.02 ± 0.03	8.01 ± 0.04	7.95 ± 0.06	$7.41^{+0.13}_{-0.12}$	$6.13^{+0.36}_{-0.18}$
	$\log(\rho_Q)$	7.65 ± 0.03	7.65 ± 0.04	7.64 ± 0.06	7.25 ± 0.12	$5.83^{+0.34}_{-0.19}$
	$\log(\rho_{SF})$	7.78 ± 0.03	7.76 ± 0.04	7.66 ± 0.06	$6.88^{+0.13}_{-0.12}$	$5.17^{+0.30}_{-0.19}$
1.5 $\leq z < 2.0$	$\log(\eta_A)$	$-2.41^{+0.37}_{-0.11}$	$-2.56^{+0.19}_{-0.08}$	-2.88 ± 0.07	-3.97 ± 0.14	$-5.76^{+0.38}_{-0.21}$
	$\log(\eta_Q)$	$-3.39^{+0.12}_{-0.04}$	$-3.40^{+0.10}_{-0.05}$	-3.48 ± 0.07	-4.29 ± 0.14	$-6.27^{+0.40}_{-0.24}$
	$\log(\eta_{SF})$	$-2.21^{+0.21}_{-0.19}$	-2.52 ± 0.11	-3.01 ± 0.07	-4.25 ± 0.14	$-6.05^{+0.26}_{-0.23}$
	$\log(\rho_A)$	$7.79^{+0.05}_{-0.03}$	$7.79^{+0.05}_{-0.04}$	7.74 ± 0.07	$7.20^{+0.14}_{-0.13}$	$5.81^{+0.39}_{-0.21}$
	$\log(\rho_Q)$	7.29 ± 0.03	7.30 ± 0.04	7.29 ± 0.07	6.88 ± 0.14	$5.29^{+0.42}_{-0.24}$
	$\log(\rho_{SF})$	7.65 ± 0.04	7.64 ± 0.05	7.56 ± 0.07	6.93 ± 0.14	$5.53^{+0.26}_{-0.23}$
2.0 $\leq z < 2.5$	$\log(\eta_A)$	$-3.06^{+0.70}_{-0.13}$	$-3.11^{+0.43}_{-0.11}$	$-3.30^{+0.16}_{-0.09}$	-4.20 ± 0.16	$-5.89^{+0.38}_{-0.26}$
	$\log(\eta_Q)$	$-3.58^{+0.35}_{-0.41}$	$-3.67^{+0.22}_{-0.30}$	$-3.91^{+0.11}_{-0.14}$	-4.82 ± 0.17	$-6.37^{+0.31}_{-0.40}$
	$\log(\eta_{SF})$	$-3.18^{+0.87}_{-0.16}$	$-3.23^{+0.52}_{-0.12}$	$-3.42^{+0.18}_{-0.09}$	-4.32 ± 0.16	$-6.04^{+0.42}_{-0.27}$
	$\log(\rho_A)$	$7.43^{+0.11}_{-0.04}$	$7.43^{+0.11}_{-0.06}$	$7.41^{+0.10}_{-0.08}$	6.98 ± 0.16	$5.69^{+0.40}_{-0.26}$
	$\log(\rho_Q)$	6.83 ± 0.07	6.82 ± 0.07	6.80 ± 0.09	6.38 ± 0.17	$5.21^{+0.32}_{-0.41}$
	$\log(\rho_{SF})$	$7.31^{+0.14}_{-0.04}$	$7.31^{+0.13}_{-0.06}$	$7.29^{+0.10}_{-0.08}$	6.86 ± 0.16	$5.53^{+0.45}_{-0.27}$
2.5 $\leq z < 3.0$	$\log(\eta_A)$	$-2.88^{+0.69}_{-0.52}$	$-3.09^{+0.41}_{-0.35}$	$-3.43^{+0.19}_{-0.18}$	-4.32 ± 0.18	$-5.57^{+0.28}_{-0.27}$
	$\log(\eta_Q)$	$-4.02^{+1.29}_{-0.68}$	$-4.05^{+0.84}_{-0.52}$	$-4.19^{+0.39}_{-0.29}$	-5.00 ± 0.20	$-6.63^{+0.45}_{-0.44}$
	$\log(\eta_{SF})$	$-2.99^{+0.84}_{-0.53}$	$-3.20^{+0.49}_{-0.35}$	$-3.55^{+0.21}_{-0.18}$	-4.42 ± 0.18	$-5.61^{+0.28}_{-0.27}$
	$\log(\rho_A)$	$7.32^{+0.13}_{-0.09}$	$7.32^{+0.13}_{-0.10}$	$7.28^{+0.12}_{-0.11}$	6.91 ± 0.18	6.04 ± 0.28
	$\log(\rho_Q)$	$6.58^{+0.29}_{-0.17}$	$6.58^{+0.27}_{-0.17}$	$6.57^{+0.22}_{-0.15}$	6.19 ± 0.20	$4.95^{+0.48}_{-0.46}$
	$\log(\rho_{SF})$	$7.21^{+0.16}_{-0.10}$	$7.21^{+0.15}_{-0.11}$	$7.17^{+0.13}_{-0.12}$	6.82 ± 0.18	6.00 ± 0.28
3.0 $\leq z < 4.0$	$\log(\eta_A)$	$-3.14^{+1.41}_{-1.25}$	$-3.65^{+0.84}_{-0.74}$	$-4.20^{+0.36}_{-0.34}$	$-5.04^{+0.22}_{-0.16}$	$-5.80^{+0.25}_{-0.24}$
	$\log(\eta_Q)$	$-5.44^{+3.26}_{-0.94}$	$-5.44^{+2.19}_{-0.67}$	$-5.46^{+1.15}_{-0.42}$	$-5.83^{+0.38}_{-0.18}$	$-6.97^{+0.69}_{-0.49}$
	$\log(\eta_{SF})$	$-3.11^{+1.47}_{-1.38}$	$-3.67^{+0.88}_{-0.81}$	$-4.27^{+0.38}_{-0.35}$	$-5.11^{+0.19}_{-0.17}$	-5.85 ± 0.24
	$\log(\rho_A)$	$6.64^{+0.43}_{-0.19}$	$6.63^{+0.31}_{-0.18}$	$6.57^{+0.20}_{-0.15}$	$6.31^{+0.21}_{-0.17}$	5.89 ± 0.26
	$\log(\rho_Q)$	$5.58^{+0.93}_{-0.22}$	$5.58^{+0.81}_{-0.22}$	$5.58^{+0.62}_{-0.20}$	$5.44^{+0.42}_{-0.19}$	$4.62^{+0.77}_{-0.53}$
	$\log(\rho_{SF})$	$6.59^{+0.49}_{-0.20}$	$6.58^{+0.34}_{-0.19}$	$6.50^{+0.19}_{-0.15}$	$6.25^{+0.19}_{-0.17}$	5.86 ± 0.27

Notes. Number densities η are in units of Mpc^{-3} , while stellar mass densities ρ are in units of $M_{\odot} \text{ Mpc}^{-3}$. Both the number and stellar mass densities are calculated for $\log(M_{\text{star}}/M_{\odot}) < 13$. The listed errors are the total 1σ errors, including Poisson uncertainties, the uncertainties from photometric redshift random errors, and cosmic variance.

the UltraVISTA measurements, a double Schechter function is required.

This implies that the decline in α with increasing redshift in the UltraVISTA SMFs is more a reflection of the changing limiting M_{star} with increasing redshift. At higher redshift, the UltraVISTA Schechter function fits become increasingly dominated by the high-mass end and do not constrain the double

Schechter function upturn. Probing further down the low-mass end will most likely result in steeper α values than have been measured with the current depth. We note that given the limiting M_{star} of the UltraVISTA SMFs and the fact that α is not well constrained at high redshift, we have also performed all the fits with fixed $\alpha = -1.2$, which is closer to the Santini et al. (2012) and UV-selected SMF measurements. These fixed- α fits

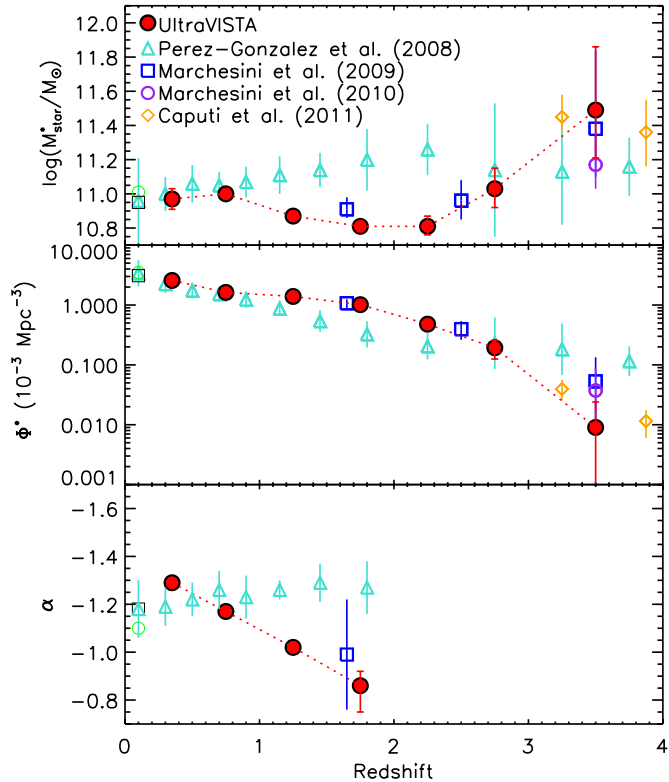


Figure 9. Best-fit Schechter parameters as a function of redshift for combined SMFs determined using the UltraVISTA data (red circles). The squares and circles are the $z = 0$ measurements from Cole et al. (2001) and Bell et al. (2003). Also shown are parameters from previous rest-frame-optical-selected SMFs from Pérez-González et al. (2008), Marchesini et al. (2009, 2010), and Caputi et al. (2011). The SMFs show little evolution in M_{\star}^* with redshift, but an evolution of $2.70^{+0.96}_{-0.42}$ dex in Φ^* since $z = 3.5$. It appears that α flattens with increasing redshift; however, this is more likely to be a result of depth of the data rather than a true flattening (see the text).

(A color version of this figure is available in the online journal.)

are incorporated into the uncertainties in quantities such as the SMDs and so these should still be representative.

If the α values of star-forming and quiescent galaxy SMFs shown in Figure 5 are representative of the α values at lower masses than are probed by the current catalog, then it suggests that the single Schechter function fit we have used will be a poor representation of the faint end at increasing redshift. Because the α values of the star-forming and quiescent SMFs are so different, and the mix of the two populations is a strong function of mass (e.g., Figure 6), a double Schechter function parameterization will be necessary to describe the faint end of the combined population below the mass limit of the current data. If so, then the flattening of α with redshift that we measure for the combined population is most likely a consequence of the fact that the mass limit of the survey is near the M_{\star} where the number densities transition between being dominated by the quiescent population to being dominated by the star-forming population. A more thorough understanding of the differences in the slope of rest-frame-optical-selected and UV-selected SMFs will have to wait until deeper rest-frame-optical data are available and can be used to select galaxies with comparable limits in stellar mass as the UV-selected samples.

5.2. The Quiescent Population

The SMF of the quiescent population shows significant evolution since $z = 3.5$. Although there is little change in M_{\star}^* ,

Φ^* has increased by $0.57^{+0.03}_{-0.04}$, $1.39^{+0.07}_{-0.07}$, and $2.75^{+0.36}_{-0.23}$ dex since $z \sim 1.0$, 2.0, and 3.5, respectively. With the improved uncertainties from UltraVISTA, there is also evidence for a steady increase in the number density of even the most massive quiescent galaxies ($\log(M_{\star}/M_{\odot}) > 11.5$) since $z = 3.5$ (Figure 8). The uncertainties from earlier studies (e.g., Brammer et al. 2011) were large enough that they could accommodate no growth in the number densities of these galaxies since $z = 2.2$.

At $z < 1$, the data are complete to a sufficiently small M_{\star} such that the upturn in the number density of quiescent galaxies at $\log(M_{\star}/M_{\odot}) < 9.5$ can be clearly seen. This upturn is also seen at $z = 0$ in the quiescent population (e.g., Bell et al. 2003; Baldry et al. 2012) and the UltraVISTA data now confirm that it persists to at least $z = 1$. In Appendix B, we show that the existence of the upturn is robust to the definition of quiescent galaxies, although its prominence can be increased or decreased depending on the strictness of the selection. Interestingly, the location of the upturn seems to evolve with mass, from $\log(M_{\star}/M_{\odot}) \sim 9.2$ at $z = 0.75$ to $\log(M_{\star}/M_{\odot}) \sim 9.5$ at $z = 0.35$.

It has been suggested that the upturn is the result of a population of star-forming satellite galaxies that have been quenched in high-density environments (e.g., Peng et al. 2010, 2012). The Peng et al. (2010) model separates the quenching process into two forms: “environmental quenching,” and “mass quenching”; the former is caused by high-density environments, and the latter is caused by processes internal to the galaxies themselves. In their model, the M_{\star} where the upturn occurs is determined by the relative α s of the mass-quenched quiescent population and the environmentally quenched quiescent population (formerly a recently star-forming population). In the case that the α values of the self-quenched quiescent populations and the star-forming populations do not evolve with redshift—which is consistent with our measurements—an evolution in the M_{\star} of the upturn would imply a change in the fraction of galaxies that self-quench as compared to those that environmentally quench. An evolution to higher masses with decreasing redshift would imply an increase in the fraction of galaxies that are environmental-quenched with decreasing redshift, i.e., environmental-quenching becomes increasingly more important at lower redshift.

It is also interesting to examine the evolution of the fraction of quiescent galaxies as a function of both M_{\star} and z . These fractions are plotted in the bottom panels of Figure 6. At $z < 1$, we recover the well-known result that quiescent galaxies dominate the high-mass end of the SMF (e.g., Bundy et al. 2006; Ilbert et al. 2010; Pozzetti et al. 2010; Brammer et al. 2011), but thereafter some interesting trends emerge.

The fraction of quiescent galaxies with $\log(M_{\star}/M_{\odot}) > 11.0$ continues to decline slowly with increasing redshift up to $z = 1.5$. After $z > 1.5$, that decline accelerates significantly and we find that by $z = 2.5$ the fraction of quiescent galaxies has decreased to the point where star-forming galaxies dominate the SMF at all stellar masses. This result is shown in Figure 10 where we plot the M_{\star} at which quiescent galaxies dominate the SMF (denoted M_{cross}) as a function of redshift. Also plotted in Figure 10 are measurements of M_{cross} from other studies (Bell et al. 2003; Bundy et al. 2006; Pozzetti et al. 2010; Baldry et al. 2012). These studies use different definitions of star-forming and quiescent galaxies, so a direct comparison with the UltraVISTA measurements is difficult; however, we note that they are largely consistent with the UltraVISTA measurements in the redshift range where the data overlap.

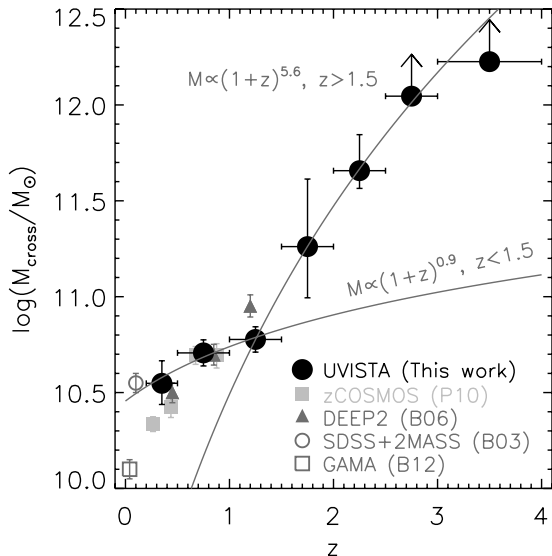


Figure 10. M_{\star} at which quiescent galaxies dominate over star-forming galaxies (M_{cross}) as a function of redshift. Measurements from other surveys are shown and agree reasonably well with the UltraVISTA measurements. Quiescent galaxies dominate the high-mass end of the SMF up to $z \sim 1.5$. Thereafter, star-forming galaxies quickly become dominant at all M_{\star} .

As Figure 10 shows, the crossing mass at $z = 0.35$ is $\log(M_{\star}/M_{\odot}) = 10.55$ and the crossing mass evolves as $\log(M_{\text{cross}}/M_{\odot}) \propto (1+z)^{0.9}$ up to $z = 1.5$. Thereafter, it evolves much more rapidly $\log(M_{\text{cross}}/M_{\odot}) \propto (1+z)^{5.6}$ up to $z = 2.5$, after which star-forming galaxies dominate the full population.

Despite the sharp change in the evolution of M_{cross} at $z = 1.5$, the overall increase in the number density of the quiescent population (i.e., Φ^*) is fairly smooth with redshift. Therefore, the rapid evolution of M_{cross} at $z > 1.5$ is really a reflection of the fact that M_{cross} moves onto the exponential part of the Schechter function at high redshift, whereas it occurs on the power-law part of the Schechter function at low redshift.

Although their fraction diminishes substantially at high redshift, it is noteworthy that we find a non-zero fraction of quiescent galaxies ($\sim 10\%-20\%$) up to $z = 3.5$. A similarly small but non-zero fraction was also found by Marchesini et al. (2010) in the NMBS. We will discuss the SEDs of the quiescent population in more detail in a future paper (D. Marchesini, in preparation), but we note that for some, the best-fit ages are ≤ 1.0 Gyr. If they formed most of their stars in a rapid burst, as suggested by the best-fit τ model, it suggests that there may be a non-zero population of quiescent galaxies that extends to as high as $z = 6\text{--}8$. Substantially deeper wide-field data (or longer wavelength selection) will be needed to find such galaxies at $z > 4$, as the K_s -band moves blueward of the Balmer break and quickly becomes inefficient at detecting red galaxies.

5.3. The Star-forming Population

Figure 5 shows that in contrast to the SMF of quiescent galaxies, the evolution of the SMF of star-forming galaxies from $z = 3.5$ to $z = 0$ is fairly modest. M_{\star}^* and α show no significant evolution up to $z = 3.5$, albeit with large uncertainties in the latter. Unlike the quiescent population, the number density of $\log(M_{\star}/M_{\odot}) > 11.5$ galaxies shows almost no evolution up to $z = 3.5$ (Figure 8). The only significant evolution is in Φ^* , which evolves by $0.45^{+0.03}_{-0.03}$, $1.01^{+0.06}_{-0.06}$, and $2.40^{+0.21}_{-0.21}$ dex since $z \sim 1.0$, 2.0, and 3.5, respectively. If we compare this to the evolution of the quiescent population at the same redshifts, we find that the

quiescent population has grown faster in Φ^* by factors of ~ 1.3 , 2.4, and 2.2 since $z \sim 1.0$, 2.0, and 3.5, respectively. This shows that at all redshifts the majority of the growth in the combined SMF is due to the increase in the quiescent population.

The non-evolution in M_{\star}^* and α and the rather slow evolution in Φ^* for the star-forming population is remarkable if considered in the context of the evolution of the SFR per unit M_{\star} (SSFR) over the same redshift range. The SSFR of star-forming galaxies with $\log(M_{\star}/M_{\odot}) = 10.0$ (11.0) declines by a factor of ~ 20 (25) since $z \sim 2$ (e.g., Muzzin et al. 2013), which means that the growth rate of these galaxies is evolving substantially with redshift. That the process of galaxy quenching evolves in such a way to keep the shape and normalization of the star-forming SMF roughly constant over this redshift range, while there is a significant decrease in the SSFRs, implies a carefully orchestrated balance between galaxy growth and quenching with redshift.

Given that with the UltraVISTA data we now have a reasonably well determined SMF at $z = 3.5$ for star-forming galaxies, it is interesting to compare this SMF with measurements of the SMFs of UV-selected star-forming galaxies. In principle, our SMF of rest-frame-optical-selected star-forming galaxies should be more complete, as both UV-bright and UV-faint star-forming galaxies will be selected, where the latter are likely to be highly dust-obscured galaxies. With few rest-frame-optical-selected SMFs for star-forming galaxies at $z > 3$ in the literature, it is still unclear how large the population of UV-faint, star-forming galaxies is.

In the left panel of Figure 11, we plot the SMF of K_s -selected star-forming galaxies at $2.0 < z < 2.5$, as well as the SMF of BM/BX-selected galaxies by Reddy & Steidel (2009). We have converted the Reddy & Steidel (2009) SMF from a Salpeter IMF to a Kroupa IMF to match UltraVISTA (N. Reddy 2013, private communication). The BM/BX galaxies typically span the redshift range $1.9 < z < 2.7$ (Reddy & Steidel 2009), which is a reasonable match to the redshift range of the K_s -selected galaxies.

Considering the sizable systematic differences that can arise from different ways of measuring the SMF (see, e.g., the inter-comparison of SMFs in the literature in the Appendix of Marchesini et al. 2009), the SMFs do agree reasonably well, particularly at the highest masses. This suggests either that the BM/BX selection effectively selects the majority of massive star-forming galaxies, regardless of their UV luminosity, or that massive dusty star-forming galaxies are less abundant than UV-bright ones at $z \sim 2.3$. Qualitatively speaking, the UVJ diagram (Figure 3) suggests that the colors of star-forming galaxies above the M_{\star} completeness limit are primarily red as compared to blue, so the high completeness of the BM/BX selection for this population is somewhat unexpected.

The low-mass end of the SMFs do not agree well; the BM/BX population is more abundant than the rest-frame-optical-selected population. This is difficult to reconcile given that we have adopted strict M_{\star} completeness limits and that the K_s selection should be more robust than UV selection. Although we cannot be conclusive, the discrepancy could arise from systematic effects due to the fact that these SMFs are determined in quite different ways. Reddy & Steidel (2009) determine the BM/BX SMF from the UV LF using a subsample of galaxies for which they have spectroscopic redshifts and SED-determined M_{\star} values. They convert the UV LF to a SMF assuming that the distribution of M_{\star} in the subsample is representative of the entire population. This is different than our approach of fitting

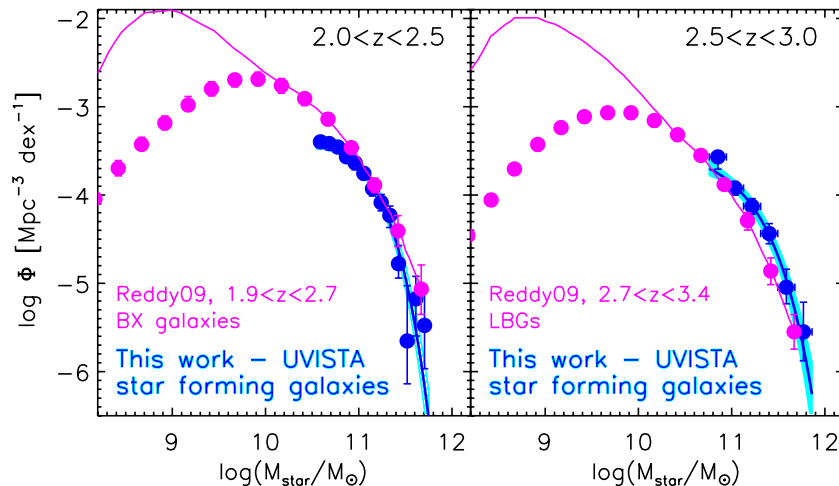


Figure 11. Left panel: comparison of the UltraVISTA star-forming SMF at $2.0 < z < 2.5$ and the BM/BX-selected SMF from Reddy & Steidel (2009). The SMFs show good agreement at the high-mass end but the UltraVISTA SMF suggests a shallower low-mass-end slope than the BM/BX SMF. Right panel: comparison of the UltraVISTA star-forming SMF at $2.5 < z < 3.0$ and the LBG-selected SMF from Reddy & Steidel (2009). These show reasonable agreement at the high-mass end, although the UltraVISTA SMF suggests that the LBG selection may miss $\sim 50\%$ of the massive galaxy population in this redshift range.

(A color version of this figure is available in the online journal.)

z_{phot} and M_{star} for each galaxy individually. Interestingly, Reddy & Steidel (2009) also determine a much steeper faint-end slope ($\alpha = -1.73 \pm 0.07$) for the SMF than other UV-selected samples that measure the SMF with z_{phot} and SED-fitting techniques similar to those used for the UltraVISTA catalog (e.g., Stark et al. 2009; González et al. 2011; Lee et al. 2012).

In the right panel of Figure 11, we compare the K_s -selected star-forming SMF at $2.5 < z < 3.0$ with the SMF of Lyman break galaxies (LBGs) from Reddy & Steidel (2009). Down to the mass limit of UltraVISTA, the shapes of those SMFs agree reasonably well, although the number density of K_s -selected star-forming galaxies is a factor of ~ 2 higher than the number density of LBGs at $\log(M_{\text{star}}/M_{\odot}) = 11.0$. Taken at face value, this result suggests the LBG selection may miss approximately half of the massive galaxies at $z > 2.5$. A similar result was also obtained by Marchesini et al. (2010), who found that only 8/14 galaxies in their mass-complete sample ($\log(M_{\text{star}}/M_{\odot}) > 11.4$) of K_s -selected galaxies at $3.0 < z < 4.0$ would be selected with U- and B-dropout selection. Using the VVDS spectroscopic sample, Le Fèvre et al. (2005) and Cucciati et al. (2012) also found that $\sim 50\%$ of the star-forming population at $z > 3$ may meet the LBG selection criteria, although we note that this result is based on a comparison of LFs, not SMFs.

In Figure 12, we expand the comparison of the K_s -selected SMFs and UV-selected SMFs using more recent determinations in the literature from Stark et al. (2009), González et al. (2011), and Lee et al. (2012). We also compare with the K_s -selected total SMF at $3.0 < z < 4.0$ determined from the MUSYC/FIREWORKS/FIRES surveys (Marchesini et al. 2009) and the NMBS (Marchesini et al. 2010), as well as the IRAC-selected SMFs in the UDS from Caputi et al. (2011). In general, most K_s -selected galaxies at this redshift are star-forming galaxies (e.g., Figure 6), so comparing the total SMFs from Marchesini et al. (2009, 2010) and Caputi et al. (2011) with the star-forming SMFs is a reasonable comparison. We note that all of the SMFs in Figure 12 have been determined with a method similar to the UltraVISTA K_s -selected catalog, e.g., z_{phot} from broadband photometry, and M_{star} from SED fitting with similar assumptions about SFHs. These SMFs have a slightly higher median redshift than the BM/BX and

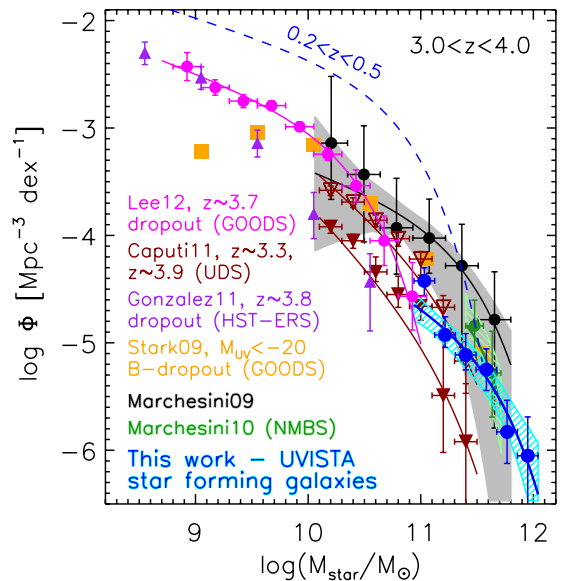


Figure 12. Comparison of the K_s -selected SMF of star-forming galaxies at $3.0 < z < 4.0$ from UltraVISTA (blue) and other SMFs in the literature. The Marchesini et al. (2009, 2010) SMFs are also K_s -selected samples and agree well with the UltraVISTA SMF. The Caputi et al. (2011) SMFs are IRAC-selected and also agree well with the UltraVISTA SMF. The Stark et al. (2009), González et al. (2011), and Lee et al. (2012) SMFs are UV selected. These agree reasonably well with UltraVISTA at $\log(M_{\text{star}}/M_{\odot}) = 11.0$, but it appears that UV selection may miss the most massive galaxies in this redshift range.

(A color version of this figure is available in the online journal.)

LBG SMFs, so we compare to the highest-redshift SMF in UltraVISTA, $3.0 < z < 4.0$.

Beginning with the K_s -selected samples, we find that, within the errors, the K_s - and IRAC-selected SMFs agree reasonably well, although the region of comparison is limited to fairly high M_{star} . Interestingly, all three show little evolution in the number density of the most massive galaxies (at $\log(M_{\text{star}}/M_{\odot}) > 11.5$) from $z = 3.5$ to $z = 0$. The largest discrepancy between the K_s -selected SMFs is for UltraVISTA and MUSYC at $\log(M_{\text{star}}/M_{\odot}) = 11.0$, where the number density

from UltraVISTA is a factor of ~ 3 less abundant in such galaxies than MUSYC. Comparison of the $1/V_{\max}$ points shows that this difference is not significant.

If confirmed, the result that the abundance of $\log(M_{\text{star}}/M_{\odot}) > 11.5$ star-forming galaxies is unchanged since $z = 3.5$ is quite interesting. We note that at the present time, we cannot be 100% confident of how real this population is. Examination of their SEDs shows that the fits are reasonable; however, they are almost all extremely red and dusty. It is also difficult to tell if emission from an AGN causes their M_{star} values to be inflated.

At present, there are no spectroscopic redshifts for such galaxies so we cannot rule out the possibility that they are extremely dusty galaxies at a lower redshift (see also the discussion in Marchesini et al. 2010). We explore this possibility further in Appendix A and find that the use of an additional very dusty template in z_{phot} fitting can reduce the number density of this population by a factor of ~ 2 . Given this, at present it may be best to consider their abundance an upper limit on the true abundance.

Returning to the UV-selected samples, comparison of the K_s -selected SMFs with the UV-selected SMFs also shows reasonable agreement in the limited mass range where the surveys overlap. At $\log(M_{\text{star}}/M_{\odot}) = 11.0$, the K_s -selected SMF lies between the Stark et al. (2009) and Lee et al. (2012) SMFs. Extrapolation of the best-fit Schechter functions of both of those samples does not agree well with the abundance of massive star-forming galaxies in UltraVISTA. A simultaneous Schechter function fit to the Lee et al. (2012) data and the UltraVISTA data does not produce a good fit. There seem to be two possible reasons for this. Either UV selection misses most of the most massive star-forming galaxies at $z > 3$ due to dust obscuration or the abundance of these galaxies is overestimated in the K_s -selected sample due to a very dusty population at lower redshift.

Overall, the SMFs of rest-frame-optical-selected samples and UV-selected samples compare reasonably well in the mass range where they overlap. There is some evidence that UV selection is not complete for galaxies with $\log(M_{\text{star}}/M_{\odot}) > 11.0$; however, spectroscopic verification of the massive population of K_s -selected galaxies will be important to verify this result.

5.4. Evolution of the Stellar Mass Density

The left panel of Figure 7 shows that the measured evolution of the SMD for the combined population is well-determined and in excellent agreement with previous determinations. Our data show that the SMD of the universe was only 50%, 10%, and 1% of its current value at $z \sim 1.0, 2.0$, and 3.5 , respectively.

The left panel of Figure 8 shows the evolution of the SMD of the quiescent and star-forming populations separately. The SMDs of these populations have evolved quite differently since $z = 3.5$, a conclusion that was already apparent from the comparison of the SMFs themselves. The SMD of star-forming galaxies increases at a rate $\rho_{\text{star}} \propto (1+z)^{-2.3 \pm 0.2}$, whereas the SMD of quiescent galaxies evolves much faster, as $\rho_{\text{star}} \propto (1+z)^{-4.7 \pm 0.4}$. This strong differential evolution in the SMD can also be seen in the inset panel of Figure 8, where we plot the fraction of the total SMD in star-forming and quiescent galaxies as a function of redshift.

As Figure 7 shows, the universe contained only $\sim 1\%$ of the total M_{star} formed by $z = 0$ at $z = 3.5$. The inset of Figure 8 shows that at that time the fraction of quiescent galaxies was small and approximately 90% of the total SMD was contained within star-forming galaxies. Since $z = 3.5$, the fraction of the SMD

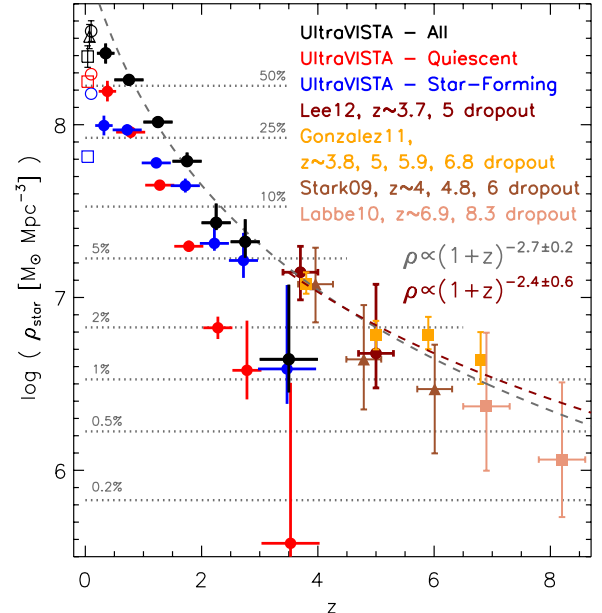


Figure 13. Evolution of the stellar mass density in the universe between $z = 0$ –8.5. The SMDs determined from UV-selected samples are shown at $z > 3.5$. Below $z < 3.5$, the K_s -selected SMDs from UltraVISTA are shown for the total (black), star-forming (blue), and quiescent (red) populations. The $z \sim 0$ data from Cole et al. (2001; triangles), Bell et al. (2003; circles), and Baldry et al. (2012; squares) are also shown. The SMD in star-forming galaxies from the K_s -selected and UV-selected samples agrees to within 1σ , suggesting that UV-selected samples account for most of the SMD at $z > 3.5$. The dashed gray curve shows a simultaneous fit to the total SMD from UltraVISTA at $z > 1.5$ and the UV-selected samples and the dashed maroon curve shows a fit to just the UV-selected samples, both of which agree well.

(A color version of this figure is available in the online journal.)

in quiescent galaxies has grown continuously and at $z \sim 0.75$ the SMD in quiescent galaxies became approximately equal to the SMD in star-forming galaxies. Perhaps coincidentally, this equality in SMD between the two types also occurs precisely at the redshift when $\sim 50\%$ of the total SMD of the universe has formed. Thereafter, the SMD in quiescent galaxies exceeds the SMD in star-forming galaxies, although we note that the details of this statement depend on the low-redshift comparison samples, as there are notable differences between the local studies of Bell et al. (2003) and Baldry et al. (2012).

Due to the superior area and depth of the UltraVISTA data, we can also compare SMDs determined from K_s -selected samples at $z = 3.5$ with those determined from UV-selected samples at the same redshift. In Figure 13, we plot the SMDs from the UltraVISTA data as well as from the UV-selected samples of Stark et al. (2009), Labb   et al. (2010), Gonz  lez et al. (2011), and Lee et al. (2012). We have also included the SMDs at $z = 0$ from Cole et al. (2001), Bell et al. (2003), and Baldry et al. (2012); the measurements of the SMD in Figure 13 span an impressive redshift baseline of $z = 0.0\text{--}8.5$.

If we compare the K_s -selected SMD at $z = 3.5$ with the UV-selected SMDs at $z \sim 3.7$ determined from Stark et al. (2009), González et al. (2011), and Lee et al. (2012) there is reasonable agreement. The SMDs from the UV-selected samples agree well with each other and are systematically ~ 0.5 dex higher than the K_s -selected measurement. The uncertainties in the K_s -selected SMD at $z = 3.5$ are quite large because the data just reach M_{star}^* and require a substantial extrapolation of the Schechter function. Although lower, the K_s -selected SMD does agree with the UV-selected SMD within the 1σ uncertainties. As shown in Figure 12, the UV-selected SMFs underpredict the

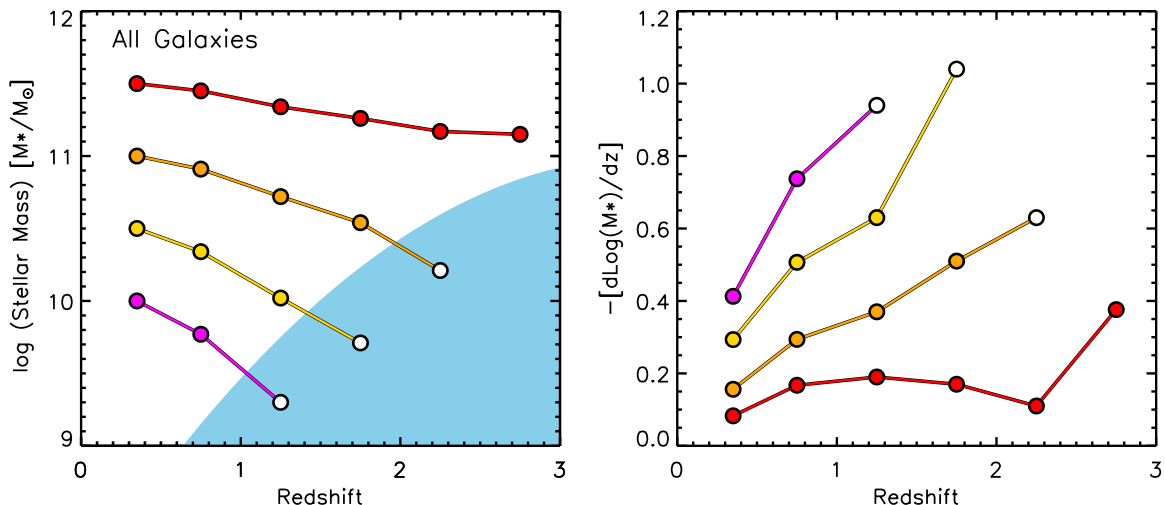


Figure 14. Left panel: average stellar mass of galaxies chosen at a fixed cumulative number density from the Schechter function fits. The cumulative number densities are chosen so that they correspond to galaxies with $\log(M_{\star,1}/M_\odot) = 11.5, 11.0, 10.5$, and 10.0 in the lowest redshift SMF. The shaded blue region represent the region that requires extrapolating the Schechter function beyond the depth of the data. Right panel: derivatives of the growth in stellar mass as a function of redshift. The derivatives separate into a sequence showing that the rate mass growth is always larger for lower mass galaxies at $z < 2$.

(A color version of this figure is available in the online journal.)

number density of the most massive galaxies, so the agreement of the total SMDs demonstrates that the total $M_{\star,1}$ contained in the most massive galaxies is negligible compared with lower mass galaxies.

The reasonable agreement between the total SMD of the K_s -selected sample and the UV-selected sample illustrates a key point, namely, that at $z > 3.5$, UV-selected samples do select samples that account for most of the SMD of the universe. Even though direct a comparison of the SMFs in Section 5.3 showed that UV selection misses approximately half of the massive star-forming galaxies and all of the massive quiescent galaxies, Figure 13 shows that the SMD in such galaxies at $z = 3.5$ is fairly small. Therefore, UV selection appears to be quite complete for the majority of star-forming galaxies at these redshifts.

Given that our results suggest that UV-selected samples should be representative of the SMD at $z > 3.5$, it seems reasonable to fit the SMD over a large redshift baseline. The SFR density shows a clear decline at $z < 1.5$ (e.g., Hopkins & Beacom 2006; Bouwens et al. 2011; Sobral et al. 2013), so we fit the data down to that redshift. Including the UV-selected samples with UltraVISTA, we find that the total SMD evolves as $\rho_{\star,1} \propto (1+z)^{-2.7 \pm 0.2}$ from $z = 8.5-1.5$. This fit is also in good agreement with a fit to just the UV-selected samples, which evolve as $\rho_{\star,1} \propto (1+z)^{-2.4 \pm 0.6}$.

The exponent in the overall fit is tantalizingly similar to the volume growth of the universe. Why the density of stars in galaxies increases at such a rate may be purely coincidental, but obviously needs to be investigated in more detail and in the context of models of galaxy evolution.

5.5. The Average Mass Growth of Galaxies

The evolution of the SMFs and SMDs illustrate the cosmological evolution of the distribution of galaxies as a function of $M_{\star,1}$ and the integrated $M_{\star,1}$ within the overall galaxy population. While important quantities from the standpoint of modeling the process of galaxy evolution, measurements of how individual galaxies assemble their mass may be more useful. Such measurements are difficult, as they requires the non-trivial task of linking galaxies and their descendants through cosmic time.

Several studies have argued that one approach for linking galaxies to their descendants is to select galaxies at a fixed constant number density (e.g., van Dokkum et al. 2010; Papovich et al. 2011). More recently, Brammer et al. (2011) argued that selecting galaxies at a fixed cumulative number density is a better approach, as it is single-valued at all $M_{\star,1}$. In a recent paper, Leja et al. (2013) tested this method on semi-analytic models (SAMs) of galaxy formation. They found that selection at a fixed cumulative number density recovered the mass evolution of the population with an accuracy of ~ 0.15 dex. They also found that the fixed cumulative number density approach may underpredict the mass growth of high-mass galaxies and overpredict the mass growth of lower-mass galaxies, although they note that this result depends on the evolution of galaxies in the SAM, which does not properly reproduce the SMF as a function of redshift.

Here, we perform fixed cumulative number density selection using the UltraVISTA SMFs in order to measure the average mass evolution of the population. We have chosen four fixed cumulative number densities to follow. These cumulative number densities are chosen to correspond to the cumulative number density for galaxies with $\log(M_{\star,1}/M_\odot) = 11.5, 11.0, 10.5$, and 10.0 , in the lowest redshift SMF bin ($0.2 < z < 0.5$).

In Figure 14, we plot $M_{\star,1}$ at these four fixed cumulative number densities out to $z = 3$. The solid shaded region in Figure 14 represents the $M_{\star,1}$ completeness limits of the survey. Cumulative number densities that require extrapolation of the Schechter function to $M_{\star,1}$ below the completeness limits are shown as open circles.

The UltraVISTA data are sufficiently complete, and the $M_{\star,1}$ evolution sufficiently slow such that we measure the mass growth of the $\log(M_{\star,1}/M_\odot) = 11.5$ population out to $z \sim 3.0$. This population demonstrates a remarkably slow growth in $M_{\star,1}$, increasing by only by 0.3 dex since $z \sim 3$ and 0.2 dex since $z \sim 2$. Using the same method, Brammer et al. (2011) measured a growth of 0.17 dex for this population since $z \sim 2$, in excellent agreement with our finding.

With the caveat that increasingly larger extrapolations are required, Figure 14 suggests that the growth of galaxies with lower $M_{\star,1}$ is always faster than galaxies with higher $M_{\star,1}$ at

$z < 2$. This can be seen more clearly in the right panel of Figure 14, where we plot the derivative of the M_{star} growth curves. These curves present a remarkable sequence at all $z < 3$, where the derivatives are always higher for lower mass galaxies.

Figure 14 encapsulates what has already been shown by many previous studies, namely that there is a “downsizing” of the galaxy population such that the highest mass galaxies assemble most of their M_{star} at high redshift, whereas lower mass galaxies grow more slowly over cosmic time. One of the most interesting implications of the curves in Figure 14 is that although low-mass galaxies grow at higher rates than higher mass galaxies at $z < 2$, they do not “overtake” their more massive counterparts. This is simply because the most massive galaxies have assembled such significant amounts of M_{star} at very early times. It also implies that at redshifts higher than those probed by the current data, the mass assembly rate of the most massive galaxies must be extremely rapid.

For example, galaxies with $\log(M_{\text{star}}/M_{\odot}) = 11.5$ at $z \sim 0.35$ have to assemble as much mass at $z < 3$ as they do at $z > 3$. The amount of cosmic time between $0 < z < 3$ is $\sim 5 \times$ more than at $3 < z < \infty$, which implies that even if those galaxies begin forming stars shortly after the big bang, their mass assembly rates must be substantially higher in the past and that they must also be substantially higher than those of low-mass galaxies at any epoch.

6. SUMMARY

In this paper, we have presented the SMFs of star-forming and quiescent galaxies to $z = 4$ using a K_s -selected catalog of the COSMOS/UltraVISTA field. The catalog is unique in terms of its large areal coverage (1.62 deg^2) and its significant depth ($K_{s,\text{tot}} = 23.4$, 90% completeness). The high quality of the data allows for arguably the best measurement of the SMFs over a large redshift baseline to date.

The total SMFs agree well with previous measurements at $0.2 < z < 3.5$, particularly at the high-mass end where the wide-field UltraVISTA data provide a substantial improvement in the statistical uncertainties. We find no significant evolution in M_{star}^* out to $z = 3.5$, although the uncertainties in M_{star}^* are large at $z > 2.5$. There is also a significant evolution in Φ^* out to $z = 3.5$. These results are also consistent with the results of Ilbert et al. (2013), who computed SMFs using UltraVISTA data. Most of the evolution in the total SMFs is driven by the quiescent population, which grows approximately twice as fast as the star-forming population at all redshifts. Integrating the SMFs, we find that the SMD of the universe was only 50%, 10%, and 1% of its current value at $z \sim 1.0$, 2.0, and 3.5, respectively.

Classification of star-forming and quiescent galaxies was performed using the rest-frame UVJ diagram. The SMFs of these populations evolve quite differently out to $z = 4$. The quiescent population evolves much faster than the star-forming population and its growth drives most of the growth in the combined SMF. The SMD contained in star-forming galaxies grows as $(1 + z)^{-2.3 \pm 0.2}$, whereas the SMD in quiescent galaxies grows much faster, as $(1 + z)^{-4.7 \pm 0.4}$. The fraction of the total SMD contained in quiescent galaxies increases with decreasing redshift and, at $z \sim 0.75$, the SMD in quiescent galaxies becomes equal to that in star-forming galaxies. This equivalence in SMD occurs at the redshift where $\sim 50\%$ of the current SMD has formed.

Starting from low redshift, we find that quiescent galaxies dominate the SMF at high masses, but that the dominance

declines to higher masses with increasing redshift. At $z > 2.5$, star-forming galaxies dominate the SMF at all stellar masses.

Comparison of the SMFs of the K_s -selected star-forming galaxies with the SMFs of UV-selected star-forming galaxies at $2.5 < z < 4.0$ shows reasonable agreement. It appears that the UV-selected samples do miss approximately half of the population of $\log(M_{\text{star}}/M_{\odot}) > 11.0$ star-forming galaxies at $z > 2.5$ due to the fact that they are very dusty; however, we note that this population of massive, dusty, star-forming galaxies does need to be spectroscopically confirmed.

Comparison of the SMDs for the K_s -selected and UV-selected samples shows that they agree within the uncertainties, which implies that even if the massive dusty population exists, it contributes relatively little to the total SMD at $z > 3.5$. This suggests that UV-selected samples at $z > 3.5$ are likely to be representative of the majority of the SMD in the universe. Given this consistency, we combined the UltraVISTA SMDs with UV-selected SMDs from the literature and fit the evolution from $1.5 < z < 8.5$. We find that the SMD evolves as $(1 + z)^{2.7 \pm 0.2}$, similar to the volume growth of the universe.

We also perform selection at a fixed cumulative number density to measure the average growth in the M_{star} of galaxies. We find that at $z < 2$, the derivatives of the M_{star} growth are always larger for lower mass galaxies, which shows that since that time galaxy growth has been mass-dependent and primarily bottom-up. In Appendices A and B, we take a closer look how the assumptions made in SED modeling affect the SMFs. We also examine the effect of the different definitions of star-forming and quiescent galaxies on the SMF.

We thank Henk Hoekstra and Remco van der Burg for generously making available the computing time for Monte Carlo simulations used in this paper. D.M. acknowledges support from program HST_AR_12141.01, provided by NASA through a grant from the Space Telescope Science Institute, which is operated by the Association of Universities for Research in Astronomy Incorporated under NASA contract NAS-26555. D.M. also acknowledges support from a Tufts University Mellon Research Fellowship in Arts and Sciences. B.M.J. and J.P.U.F. acknowledge support from the ERC-StG grant EGGS-278202. The Dark Cosmology Centre is funded by the Danish National Research Foundation. J.S.D. acknowledges the support of the European Research Council through the award of an Advanced Grant and the support of the Royal Society via a Wolfson Research Merit Award.

APPENDIX A

THE EFFECT OF SPS MODELS, METALLICITY, AND STAR FORMATION HISTORY ON THE SMF

The determination of stellar masses from SED modeling requires making assumptions about various quantities that are not well constrained by broadband photometry alone, such as the SFH, dust attenuation law, and metallicity. Depending on the assumptions made, systematically different estimates of M_{star} (e.g., Maraston et al. 2006; Muzzin et al. 2009a, 2009b; Conroy et al. 2009) and the SMF (e.g., Marchesini et al. 2009) can result for a given dataset. Previous work has shown that typically the largest systematic uncertainties in M_{star} and the overall SMF arise from the choice of the SPS model (e.g., Marchesini et al. 2009; Muzzin et al. 2009a), with the choice of metallicity and dust attenuation law contributing smaller, although not unimportant, sources of systematic error. In one of

the first works to do a careful study of these systematic errors, Marchesini et al. (2009) found that systematic uncertainties in the SMF from the MUSYC survey were approximately as large a contribution to the overall error budget as the random errors. Given that the UltraVISTA dataset covers an area >10 times larger than the MUSYC survey and has superior photometric data, we re-examine in this Appendix the possible sources of systematic uncertainties on the SMF, with the expectation that they are likely to dominate the overall error budget.

We explore four different possible sources of systematic error. For each case considered, we re-perform the SED fitting, generating a completely new catalog of M_{\star} for each galaxy. The first source of systematic error we test is to change the SPS model from BC03 to the models of Maraston (2005), hereafter M05. The M05 models have a different treatment of the thermally pulsating asymptotic horizontal branch stars (TP-AGB) which, amongst other differences with BC03, causes them to produce M_{\star} values that are typically a factor of ~ 0.65 lower than those of the BC03 models (e.g., Wuyts et al. 2007; Muzzin et al. 2009a; Marchesini et al. 2009). Whether these models are a better treatment of this phase remains an open issue (e.g., Kriek et al. 2010; Zibetti et al. 2013).

We also explore the effect of leaving metallicity as a free parameter. The FAST code allows four different metallicities for the BC03 models, $Z = 0.004, 0.008, 0.02,$ and 0.05 , which span a range of sub-solar to super-solar. We also explore the effect of using a different SFH. Maraston et al. (2010) showed that exponential-declining models were likely an overestimate of the M_{\star} for star-forming galaxies. In order to allow for an increasing SFH, we explore the effect of the “delayed τ -model” option in FAST. The delayed- τ model is a SFH of the form $SFR \propto t \times e^{-t/\tau}$, which begins with a smoother growth in the SFH before the exponential decline.

Lastly, we explore the effect of using an additional very red, “old and dusty” template in EAZY when fitting z_{phot} . Using NIR medium band data from the NMBS, Marchesini et al. (2010) found that the inclusion of such a template caused approximately half of the massive galaxies population at $z > 3$ to be consistent with a somewhat lower z_{phot} in the range $2 < z < 3$. At present, there is no strong evidence from spectroscopic samples that such an old and dusty population exists; however, there are clearly strong selection biases against obtaining successful spectroscopic redshifts for such a population if it were to exist (i.e., both age and dust make the detection of emission lines unlikely). Given the prevalence of such red SEDs at the high-mass end of the SMF at high redshift, such a template could be important and is worth examining as a potential systematic effect on the SMFs.

In Figures 15–17, we plot the SMFs derived using these different modeling assumptions for the quiescent, star-forming, and combined galaxy populations, respectively. The panels are organized by row in increasing redshift bins and below the SMFs in each redshift bin we plot the residuals compared with the default SMF. Within the panels, the shaded region represents the formal uncertainties in the default SMF. The data points are the SMFs determined with the $1/V_{\max}$ method and the solid curves represent the best-fit maximum-likelihood Schechter functions. The parameters from all SMFs are listed in Table 3.

Starting with a comparison of the SMFs for the quiescent galaxies in Figure 15, it is clear that overall the SMFs with the different models are reasonably comparable. There are some clear differences for given assumptions and in specific ranges of M_{\star} and z that stand out in the plots of the residuals. Near

the high-mass end, the residuals in Φ^* can be large, but it is important to note that because we have compared the residuals as a function of Φ^* and not M_{\star} , these can appear extremely large at the exponential tail where a small change in M_{\star} results in a significant change in Φ^* .

The two parameters that have little effect on the quiescent SMFs are the use of the dusty template and the different SFH. Quiescent galaxies are typically quite old and mostly dust-free, so it is unsurprising that the precise choice of SFH at early times and the allowance of extra dust are not important in the SED modeling.

The allowance of metallicity as a free parameter also has little effect at the high-mass end of the SMF, but does reduce the number density of very low-mass quiescent galaxies. This has the effect of reducing the significance of the upturn in the quiescent SMF seen at the lowest masses in the low-redshift bins.

As expected, the most significant systematic effect on the SMF comes from using the M05 models instead of the BC03 models. At high redshift, the effect is extremely pronounced and values of M_{\star} are typically a factor of ~ 2 lower. The effect at higher redshift is expected given that quiescent galaxies are younger there and the TP-AGB phase is most apparent when stellar populations are 0.5–2.0 Gyr in age (M05). The effect on the SMF from the SPS models diminishes with redshift; however, quite surprisingly the M05 models still produce lower number densities at the high-mass end at low redshift. Given that the BC03 and M05 models are fairly similar at old ages, it suggests that the best-fit M05 models fit substantially lower ages for massive low-redshift galaxies than the BC03 models.

In Figure 16, the SMFs for the star-forming population are plotted. Figure 16 shows that, similar to the quiescent galaxies, the choice of SFH has little effect on their SMFs. Allowing metallicity as a free parameter also does not change the SMFs within the random uncertainties. As expected, including the dusty template does have a noticeable effect at the high-mass end of the star-forming SMF at high redshift. In both the $2.5 < z < 3.0$ and the $3.0 < z < 4.0$ bins including the dusty templates reduces the number density of $\log(M_{\star}/M_{\odot}) > 11.0$ galaxies by 0.2–0.4 dex. This is fully consistent with Marchesini et al. (2010), who found that approximately half of their sample of such galaxies was consistent with a lower redshift solution. If these galaxies truly are very dusty galaxies at lower redshift, it could alleviate some of the tension between the measured SMF and the predicted SMFs from models at the high-mass end. It is clear that obtaining spectroscopic redshifts and confirmation of the M_{\star} values for this population is an important task for future observations. Unfortunately, as discussed in the text, these galaxies are faint and have extremely red SEDs. They are usually only well-detected in bands redward of the H -band. Unless they have very strong emission lines that are not completely obscured, obtaining redshifts will be challenging.

In Figure 17, the SMFs for the combined population are plotted. These reflect most of the same trends as were already pointed out in the star-forming and quiescent SMFs. In summary, we find that for the four sources of systematic error we have considered, it appears that two have an impact on the SMFs that is larger than the random uncertainties, whereas the other two do not. The choice of SFH appears to have little effect on the SMFs of any type. Furthermore, allowing metallicity as a free parameter does not affect the SMFs in any notable way other than reducing the size of the upturn of the quiescent SMF

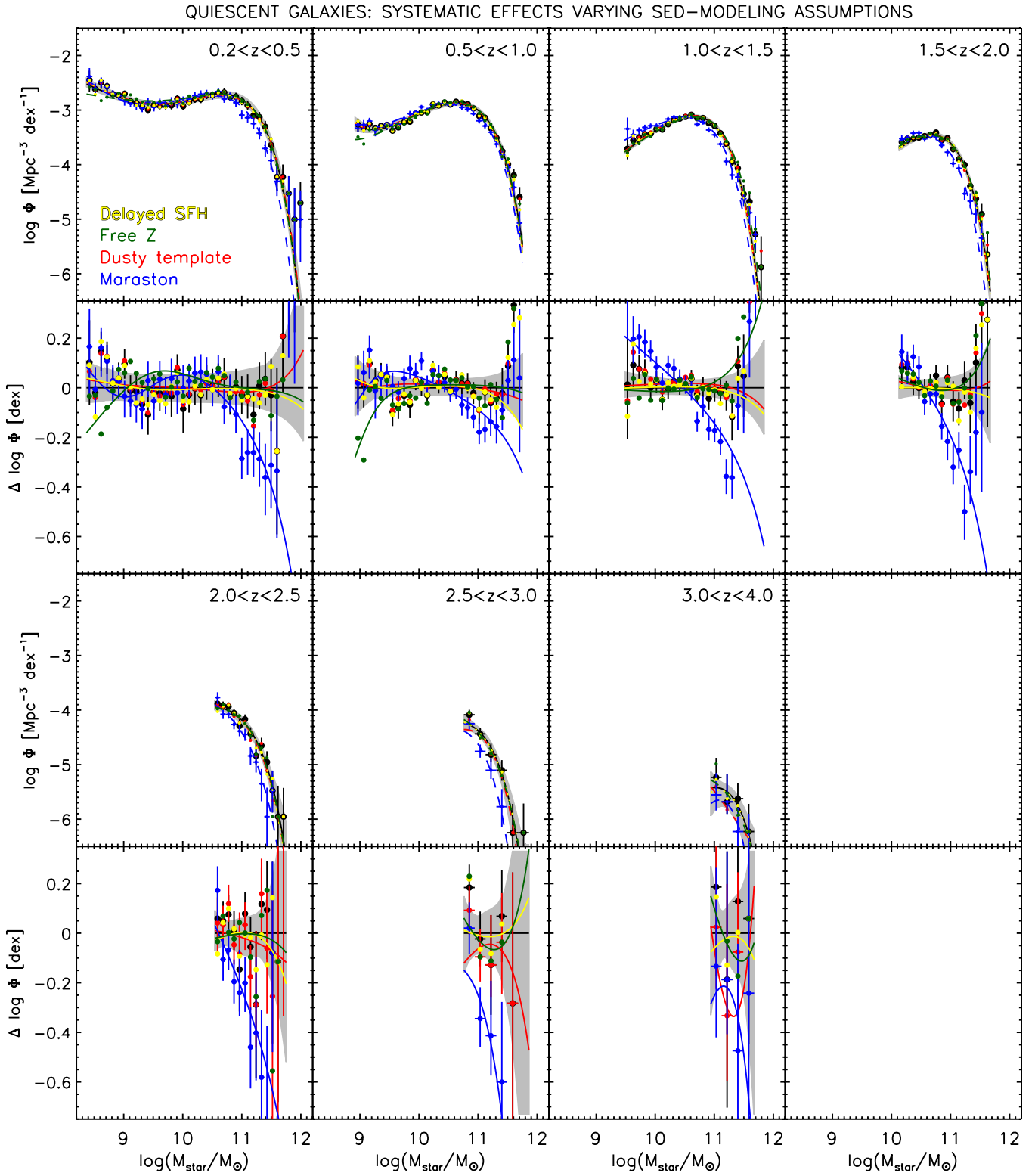


Figure 15. First and third rows: stellar mass functions for quiescent galaxies in different redshift bins. The stellar mass functions have been determined using the different SED modeling assumptions in the legend (see the text for details). Second and fourth rows: difference in measured number density at a given stellar mass compared to the default SMF. The shaded region represents the formal uncertainty (including Poisson noise, cosmic variance, and modeling errors) in the default mass function. The use of the Maraston models and a free metallicity affect the quiescent SMFs at levels larger than the formal uncertainties, but the dusty template and different SFH do not.

(A color version of this figure is available in the online journal.)

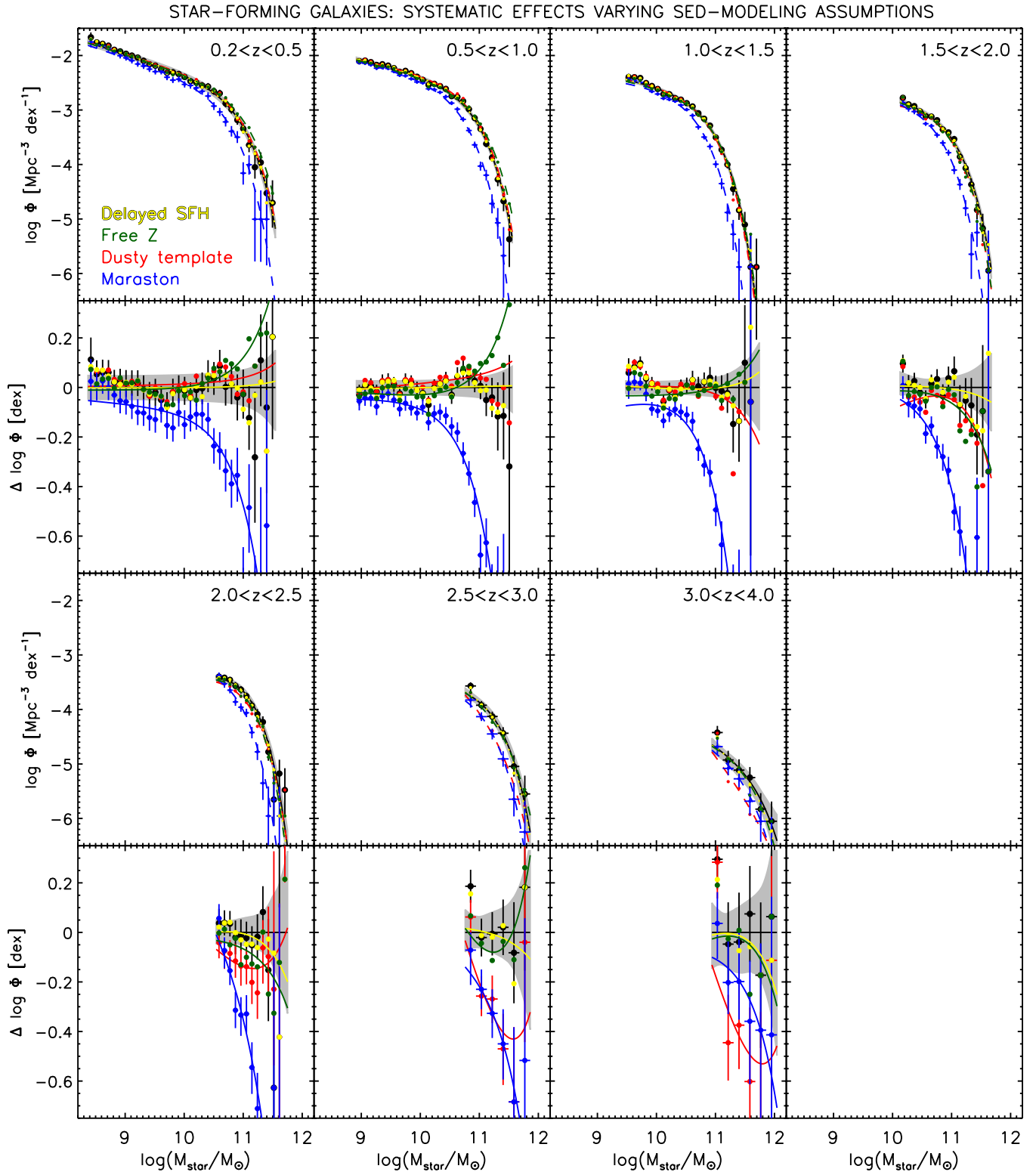


Figure 16. As in Figure 15, but for star-forming galaxies. The stellar mass function of star-forming galaxies is not affected by free metallicity or a different SFH. The SMF is affected by the use of the Maraston models at all redshifts and at the highest redshift the use of the dusty template reduces the number density of massive star-forming galaxies.

(A color version of this figure is available in the online journal.)

at very low M_{star} . This has very little effect on the combined SMF, because star-forming galaxies dominate at low M_{star} .

The two areas for concern for the SMFs in terms of systematic uncertainties are the potential dusty massive galaxies at high redshift and the SPS models. Because star-forming galaxies

dominate the SMF at all M_{star} at $z > 2.5$, the possibility that some of these galaxies are lower redshift dusty sources has serious consequences for the high-mass end of the SMF at high redshift. Lastly, it has been well-known for several years now that the choice of SPS model is the most significant systematic

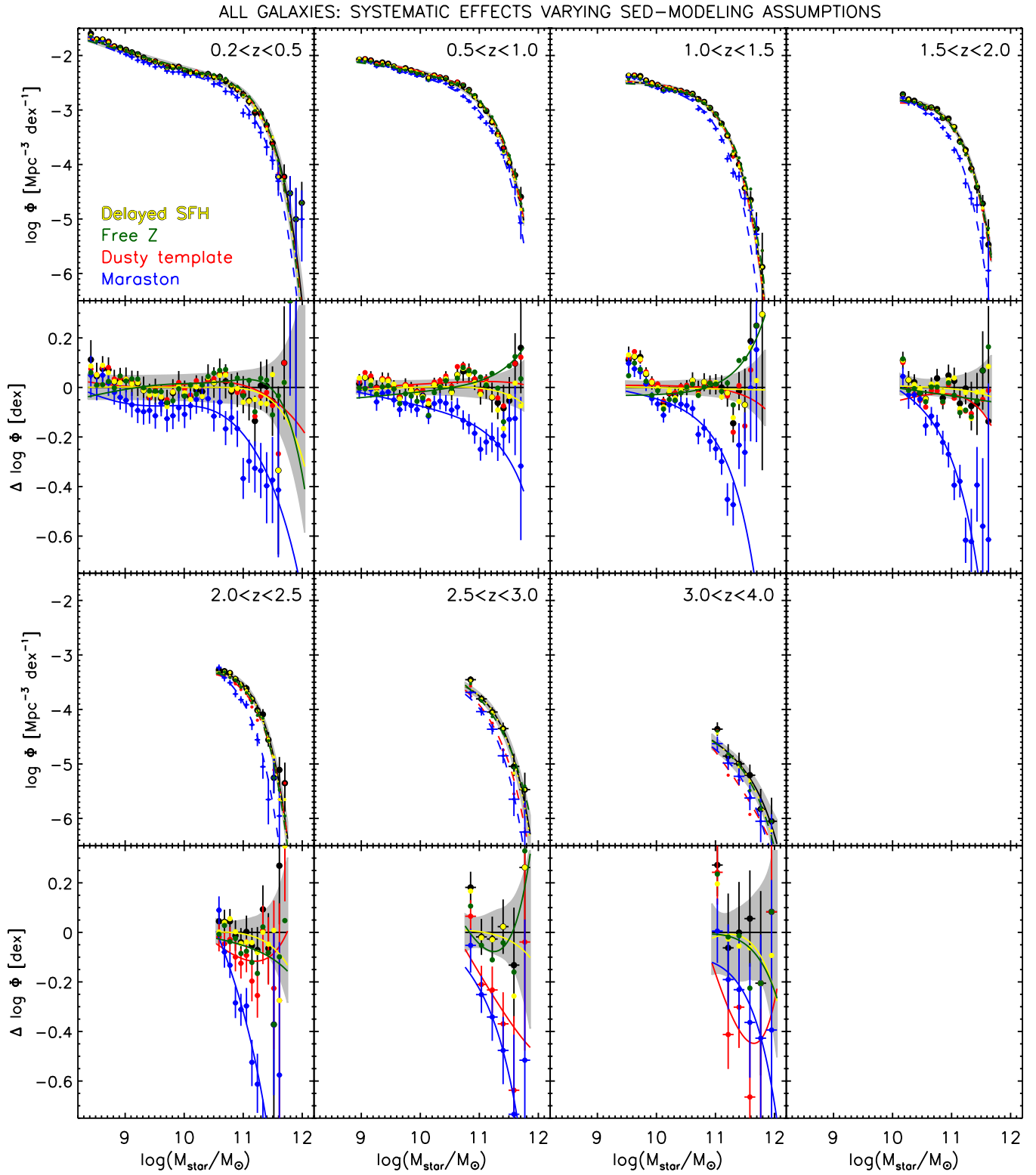


Figure 17. As in Figure 15, but for the combined population. Again, the Maraston models and the dusty template have the largest impact on the SMFs.
 (A color version of this figure is available in the online journal.)

uncertainty in the determination of M_{star} and the SMF. Using the best data available at the time, Marchesini et al. (2009) showed that this uncertainty was at least as large as the random uncertainties in the data and Marchesini et al. (2010) showed that it was the dominant source of error in the NMBS SMF. With

a substantially larger survey like UltraVISTA, it is clear that we are now completely in the regime where the SPS uncertainties dominate the total error budget in the SMFs. Resolving this issue will be critical in order to better test models of galaxy formation at all redshifts.

Table 3
Best-fit Schechter Function Parameters of the SMFs: Different SED Modeling Assumptions

Redshift	Sample	Number	$\log M_{\star}^*$ (M_{\odot})	Φ^* (10^{-4} Mpc^{-3})	α	Φ_2^* (10^{-4} Mpc^{-3})	α_2
0.2 $\leq z < 0.5$	A,SFH	18511	11.22 $^{+0.02}_{-0.03}$	12.13 $^{+0.83}_{-0.45}$	-1.29 ± 0.01
0.2 $\leq z < 0.5$	A,MET	18644	11.20 $^{+0.03}_{-0.02}$	13.98 $^{+0.79}_{-0.55}$	-1.26 ± 0.01
0.2 $\leq z < 0.5$	A,DUSTY	18885	11.20 $^{+0.02}_{-0.03}$	12.80 $^{+0.81}_{-0.47}$	-1.28 ± 0.01
0.2 $\leq z < 0.5$	A,MA05	15543	11.10 $^{+0.03}_{-0.03}$	10.65 $^{+0.46}_{-0.65}$	-1.30 ± 0.01
0.2 $\leq z < 0.5$	A,SFH	18511	11.06 ± 0.01	18.98 ± 0.14	-1.2
0.2 $\leq z < 0.5$	A,MET	18644	11.10 ± 0.01	18.63 ± 0.14	-1.2
0.2 $\leq z < 0.5$	A,DUSTY	18885	11.05 ± 0.01	19.51 $^{+0.07}_{-0.14}$	-1.2
0.2 $\leq z < 0.5$	A,MA05	15543	11.93 ± 0.01	17.58 ± 0.14	-1.2
0.2 $\leq z < 0.5$	A,SFH	18511	10.94 $^{+0.11}_{-0.05}$	17.21 $^{+3.29}_{-2.55}$	-0.47 $^{+0.16}_{-0.37}$	10.02 $^{+2.12}_{-5.66}$	-1.37 $^{+0.03}_{-0.10}$
0.2 $\leq z < 0.5$	A,MET	18644	10.91 $^{+0.08}_{-0.03}$	17.80 $^{+2.43}_{-4.24}$	-0.27 $^{+0.11}_{-0.32}$	12.94 $^{+3.35}_{-4.20}$	-1.31 $^{+0.03}_{-0.03}$
0.2 $\leq z < 0.5$	A,DUSTY	18885	10.96 ± 0.08	19.56 $^{+1.87}_{-4.61}$	-0.68 $^{+0.32}_{-0.22}$	7.25 $^{+5.22}_{-2.69}$	-1.42 ± 0.06
0.2 $\leq z < 0.5$	A,MA05	15543	10.94 ± 0.05	15.23 $^{+1.64}_{-2.44}$	-0.93 $^{+0.21}_{-0.11}$	3.23 $^{+4.05}_{-0.52}$	-1.53 $^{+0.10}_{-0.05}$
0.2 $\leq z < 0.5$	Q,SFH	4360	11.20 ± 0.03	10.09 $^{+0.56}_{-0.52}$	-0.92 ± 0.02
0.2 $\leq z < 0.5$	Q,MET	4505	11.14 ± 0.03	12.21 $^{+0.77}_{-0.55}$	-0.87 ± 0.02
0.2 $\leq z < 0.5$	Q,DUSTY	4362	11.20 ± 0.03	9.97 ± 0.54	-0.93 ± 0.02
0.2 $\leq z < 0.5$	Q,MA05	4135	11.07 ± 0.03	10.18 $^{+0.67}_{-0.51}$	-0.92 ± 0.02
0.2 $\leq z < 0.5$	Q,SFH	4360	10.75 ± 0.01	30.63 $^{+0.03}_{-0.02}$	-0.4
0.2 $\leq z < 0.5$	Q,MET	4505	10.75 ± 0.02	31.66 ± 0.02	-0.4
0.2 $\leq z < 0.5$	Q,DUSTY	4362	10.74 ± 0.01	30.67 $^{+0.03}_{-0.02}$	-0.4
0.2 $\leq z < 0.5$	Q,MARASTON	4135	10.63 ± 0.01	29.38 $^{+0.02}_{-0.03}$	-0.4
0.2 $\leq z < 0.5$	Q,SFH	4360	10.92 $^{+0.05}_{-0.03}$	19.73 $^{+1.23}_{-1.56}$	-0.38 ± 0.11	0.48 $^{+0.36}_{-0.21}$	-1.57 ± 0.11
0.2 $\leq z < 0.5$	Q,MET	4505	10.92 $^{+0.05}_{-0.03}$	18.25 $^{+1.76}_{-1.90}$	-0.32 $^{+0.11}_{-0.16}$	2.26 $^{+0.29}_{-1.16}$	-1.22 ± 0.11
0.2 $\leq z < 0.5$	Q,DUSTY	4362	10.94 $^{+0.03}_{-0.05}$	18.62 $^{+1.63}_{-1.13}$	-0.43 $^{+0.11}_{-0.05}$	0.45 $^{+0.34}_{-0.20}$	-1.57 ± 0.11
0.2 $\leq z < 0.5$	Q,MARASTON	4135	10.86 $^{+0.03}_{-0.05}$	17.25 $^{+1.82}_{-0.60}$	-0.59 ± 0.11	0.06 $^{+0.13}_{-0.01}$	-1.95 ± 0.21
0.2 $\leq z < 0.5$	SF,SFH	14151	10.82 ± 0.03	11.26 $^{+0.70}_{-0.72}$	-1.34 ± 0.01
0.2 $\leq z < 0.5$	SF,MET	14139	10.91 ± 0.03	10.28 $^{+0.65}_{-0.67}$	-1.34 ± 0.01
0.2 $\leq z < 0.5$	SF,DUSTY	14523	10.83 ± 0.03	11.64 $^{+0.93}_{-0.68}$	-1.33 ± 0.02
0.2 $\leq z < 0.5$	SF,MA05	11408	10.62 ± 0.04	10.47 $^{+0.93}_{-0.66}$	-1.36 ± 0.02
0.2 $\leq z < 0.5$	SF,SFH	14151	10.76 ± 0.02	13.42 $^{+0.20}_{-0.13}$	-1.3
0.2 $\leq z < 0.5$	SF,MET	14139	10.85 ± 0.02	12.35 $^{+0.18}_{-0.12}$	-1.3
0.2 $\leq z < 0.5$	SF,DUSTY	14523	10.78 ± 0.02	13.57 $^{+0.13}_{-0.20}$	-1.3
0.2 $\leq z < 0.5$	SF,MARASTON	11408	10.54 ± 0.02	13.49 $^{+0.21}_{-0.14}$	-1.3

(This table is available in its entirety in a machine-readable form in the online journal. A portion is shown here for guidance regarding its form and content.)

APPENDIX B

THE EFFECT OF DIFFERENT SEPARATION BETWEEN STAR-FORMING AND QUIESCENT GALAXIES ON THE SMF

Although there are now several determinations of the SMFs of star-forming and quiescent galaxies in the literature (e.g., Ilbert et al. 2010; Brammer et al. 2011; Domínguez Sánchez et al. 2011; Moustakas et al. 2013), the systematic uncertainties in these SMFs due to the definition of “quiescence” has not been examined in detail. Indeed, given that galaxies exhibit a range of SSFRs (e.g., Muzzin et al. 2013; Noeske et al. 2007; Whitaker et al. 2012) and that there is a “green valley” in the color–magnitude relation, placing galaxies within a binary definition is implicitly an oversimplification of the problem. Here, we test how varying the definition of star-forming and quiescent galaxies affects the SMFs of these types.

In order to conduct this test, we vary the bounds of the quiescent population within the UVJ diagram by ± 0.1 mag in both $U - V$ and $V - J$. Figure 18 shows an illustration of

how the variation of these bounds appears in the UVJ diagram. As Figure 18 shows, an alteration of ± 0.1 mag in color is a rather extreme test; however, we have chosen to do so in order to see what the maximum systematic uncertainties will be and how robust the results from the default model are.

In Figures 19 and 20, we plot the SMFs generated using the new UVJ definition for the quiescent and star-forming galaxies. Again, similar to the figures about the assumptions in SED modeling, we have included middle panels that show the change in Φ^* relative to the default model. All SMFs derived with the different UVJ selection are listed in Table 4.

Examining the SMFs for the quiescent population, it is clear that the definition of quiescence is quite important in the determination of the SMF. Interestingly, it is much more important for galaxies with $\log(M_{\star}/M_{\odot}) < 11.0$ than galaxies with $\log(M_{\star}/M_{\odot}) > 11.0$. This is because the most massive galaxies are the most unambiguously quiescent. Typically, they are the ones with the reddest $U - V$ colors within the quiescent box in the UVJ diagram and therefore variations in the box do not change their classification or number density. Figure 19

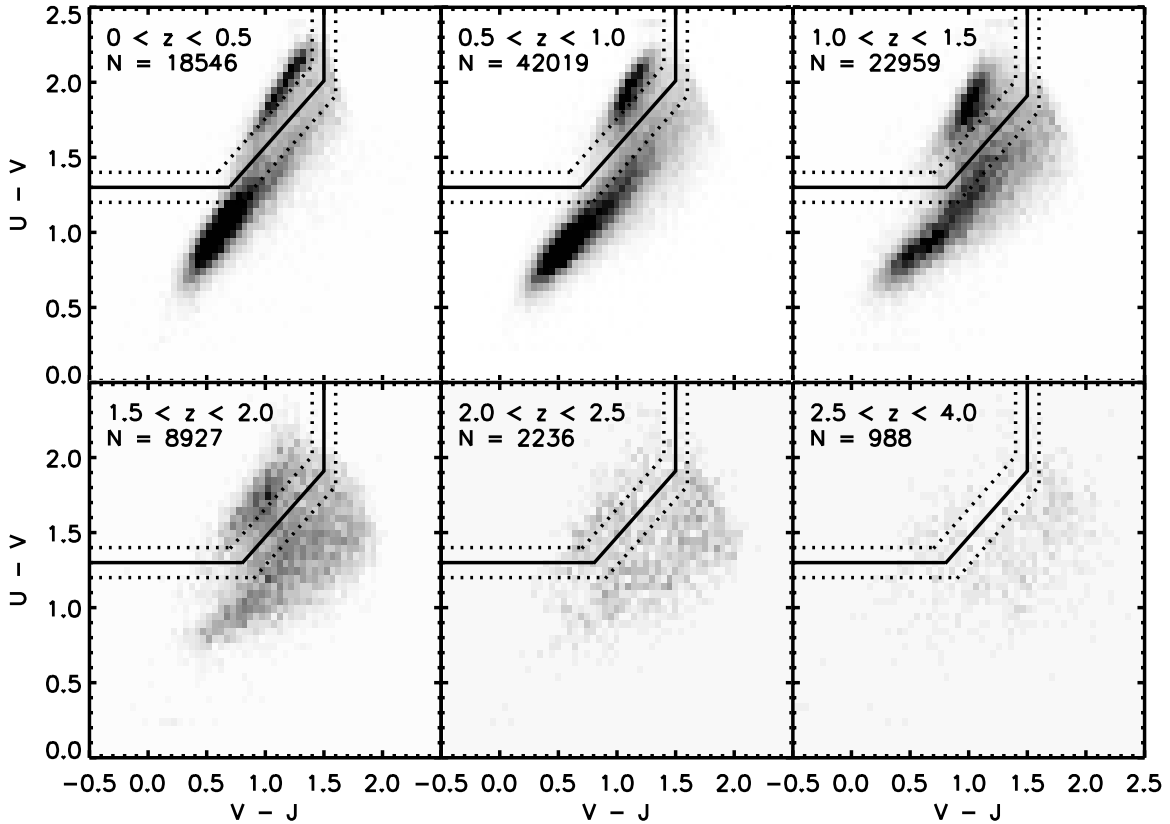


Figure 18. *UVJ* diagram as in Figure 3, but with the varied definitions of quiescent galaxies shown as the dotted line. The dotted lines represent extreme definitions of star-forming and quiescent galaxies, but therefore bracket the full range of possible stellar mass functions for these populations.

Table 4
Best-fit Schechter Function Parameters of the SMFs: Different *UVJ* Selection

Redshift	Sample	Number	$\log M_{\text{star}}^*$ (M_{\odot})	Φ^* (10^{-4} Mpc^{-3})	α	Φ_2^* (10^{-4} Mpc^{-3})	α_2
0.2 $\leq z < 0.5$	Q,UVpVJm	2489	11.13 ± 0.03	$9.86^{+0.49}_{-0.58}$	-0.72 ± 0.03
0.2 $\leq z < 0.5$	Q,UVmVJp	6769	11.18 ± 0.03	$12.38^{+0.70}_{-0.52}$	-1.00 ± 0.02
0.2 $\leq z < 0.5$	Q,UVpVJm	2489	10.89 ± 0.01	17.30 ± 0.02	-0.4
0.2 $\leq z < 0.5$	Q,UVmVJp	6769	10.64 ± 0.01	48.05 ± 0.03	-0.4
0.2 $\leq z < 0.5$	Q,UVpVJm	2489	$10.94^{+0.05}_{-0.03}$	$14.56^{+0.77}_{-1.19}$	-0.33 ± 0.11	$0.24^{+0.49}_{-0.19}$	$-1.48^{+0.21}_{-0.26}$
0.2 $\leq z < 0.5$	Q,UVmVJp	6769	$10.92^{+0.05}_{-0.03}$	$23.55^{+1.91}_{-1.83}$	-0.48 ± 0.11	$1.29^{+1.03}_{-0.61}$	-1.48 ± 0.11
0.2 $\leq z < 0.5$	SF,UVpVJm	16057	10.94 ± 0.03	$11.48^{+0.72}_{-0.69}$	-1.33 ± 0.01
0.2 $\leq z < 0.5$	SF,UVmVJp	11777	10.68 ± 0.04	$9.86^{+0.83}_{-0.69}$	-1.37 ± 0.02
0.2 $\leq z < 0.5$	SF,UVpVJm	16057	10.89 ± 0.01	$13.51^{+0.15}_{-0.13}$	-1.3
0.2 $\leq z < 0.5$	SF,UVmVJp	11777	10.58 ± 0.02	$13.43^{+0.14}_{-0.21}$	-1.3

Notes. “UVpVJm” corresponds to shifting the *UVJ* selection box by +0.1 mag in *U-V* and -0.1 mag in *V-J*; “UVmVJp” corresponds to shifting the *UVJ* selection box by -0.1 mag in *U-V* and +0.1 mag in *V-J*. The listed errors are the 1σ Poisson errors.

(This table is available in its entirety in a machine-readable form in the online journal. A portion is shown here for guidance regarding its form and content.)

shows that the change in the number density of galaxies with $\log(M_{\text{star}}/M_{\odot}) < 11.0$ is a clear function of M_{star} and can reach as high as 0.2–0.4 dex at the lowest masses probed. This change is a reflection of the colors of this population, which are bluer than the more massive population, and hence their definition as quiescent is more ambiguous.

Examination of the SMFs for the star-forming population with the different *UVJ* selection criteria (Figure 20) shows opposite trends as the quiescent population. The number densities of the lowest mass galaxies are mostly unchanged, whereas the number

densities at the highest masses can change by 0.2–0.6 dex. This is again a reflection of the fact that the colors of the lowest mass galaxies are typically very blue, making their classification as star-forming galaxies unambiguous, whereas the most massive star-forming galaxies have more intermediate colors, making their classification less clear. This comparison of SMFs makes clear that there are issues of interpretation when dividing the spectrum of galaxy SSFRs into a binary classification scheme of star forming and quiescent. It shows that comparing the observed SMFs of star-forming and quiescent galaxies with SMFs from

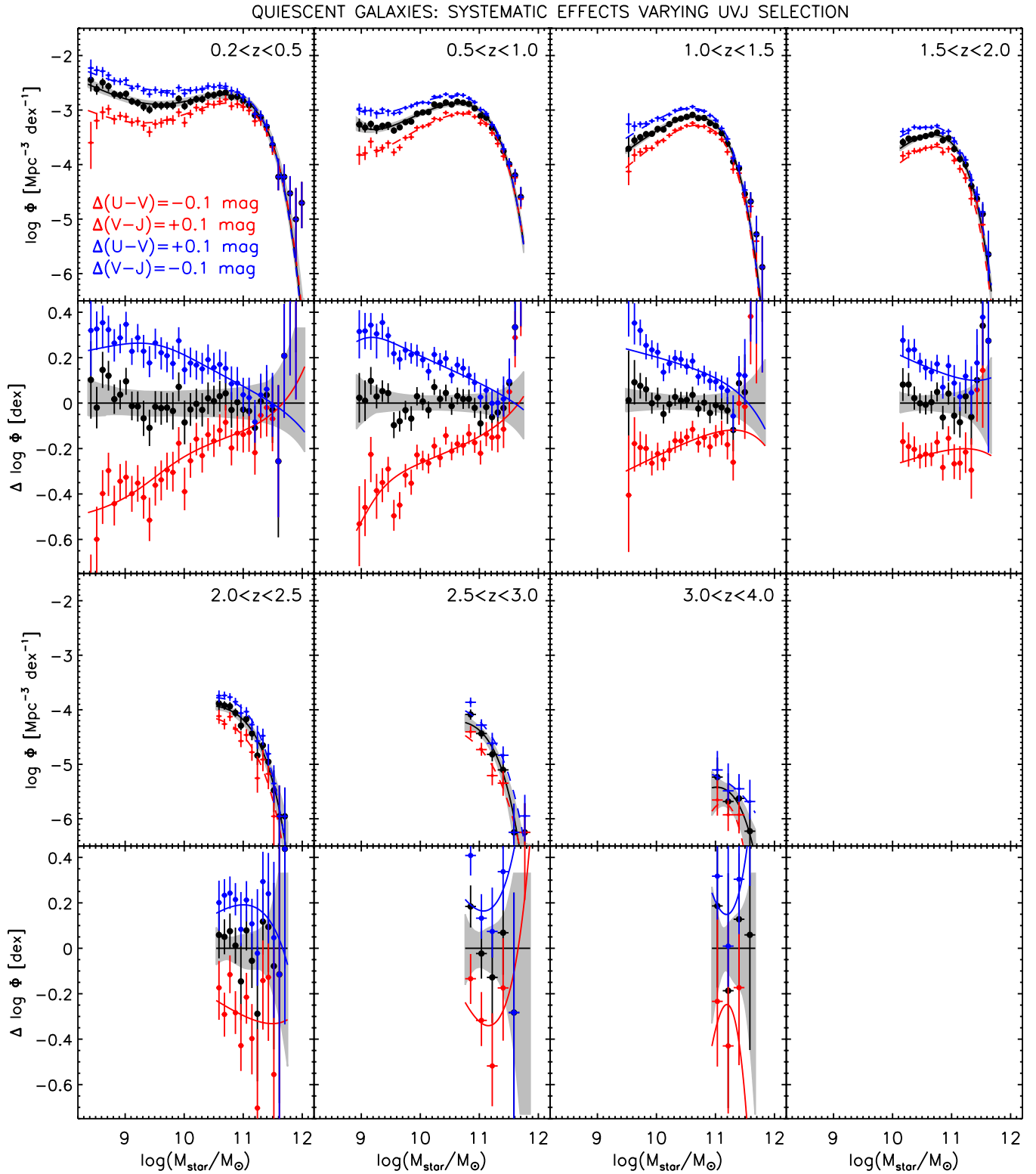


Figure 19. As in Figure 15 but for quiescent galaxies with two different definitions of star-forming and quiescent galaxies. Varying the selection has a much stronger effect on the derived mass functions for high masses than low masses because high-mass galaxies are the most quiescent.

(A color version of this figure is available in the online journal.)

models of galaxy formation requires a careful matching of definitions.

One result that appears to be robust to the definition of quiescent is the trend of an increasing fraction of quiescent

galaxies as a function of M_{star} and a decrease with z . In Figure 21, we again plot the SMFs of quiescent galaxies with the different UVJ selection, but show the quiescence fractions in the middle panels. No matter how quiescence is defined, the trend that more

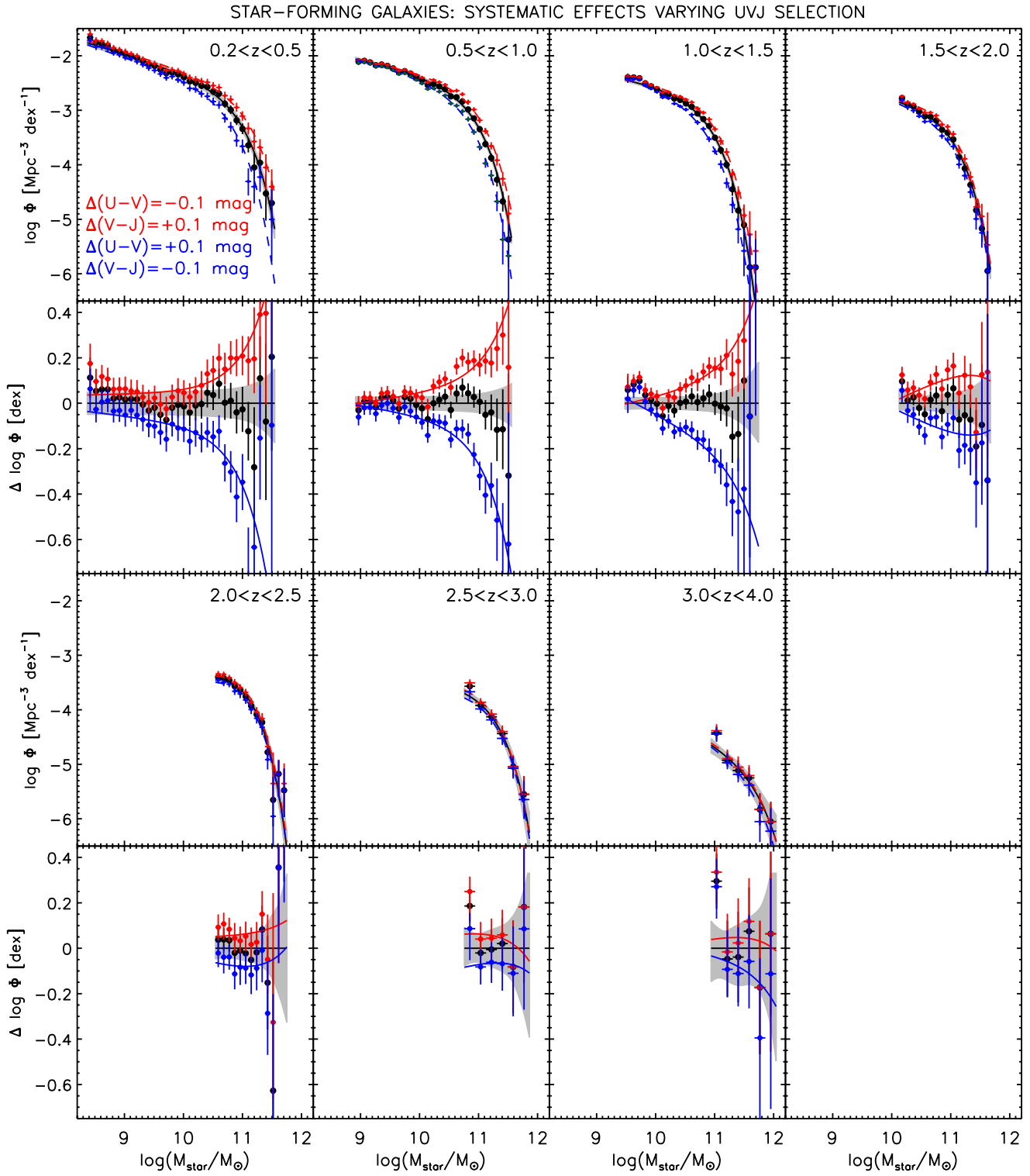


Figure 20. As in Figure 15 but for star-forming galaxies with two different definitions of star-forming and quiescent galaxies. The effect of different definitions of quiescence on the star-forming population is opposite to that on quiescent galaxies. Low-mass galaxies are not affected because they have the highest SSFRs, whereas the most massive star-forming galaxies have much lower SSFRs.

(A color version of this figure is available in the online journal.)

massive galaxies are more frequently quiescent than lower mass galaxies at $z < 2.0$ holds. Furthermore, the fact that this trend seems to disappear and that our conclusion that star-forming galaxies dominate the SMF at all M_{star} at $z > 2.5$ appear to both hold, no matter the definition of quiescence. It appears that at $z > 2.5$, there are very few galaxies consistent with being quiescent, no matter which definition is adopted.

APPENDIX C

COMPARISON WITH ILBERT ET AL. STELLAR MASS FUNCTIONS

Recently, Ilbert et al. (2013, hereafter I13) also computed the SMFs of star-forming and quiescent galaxies up to $z = 4$ based on an independently generated 30 band, PSF-matched catalog

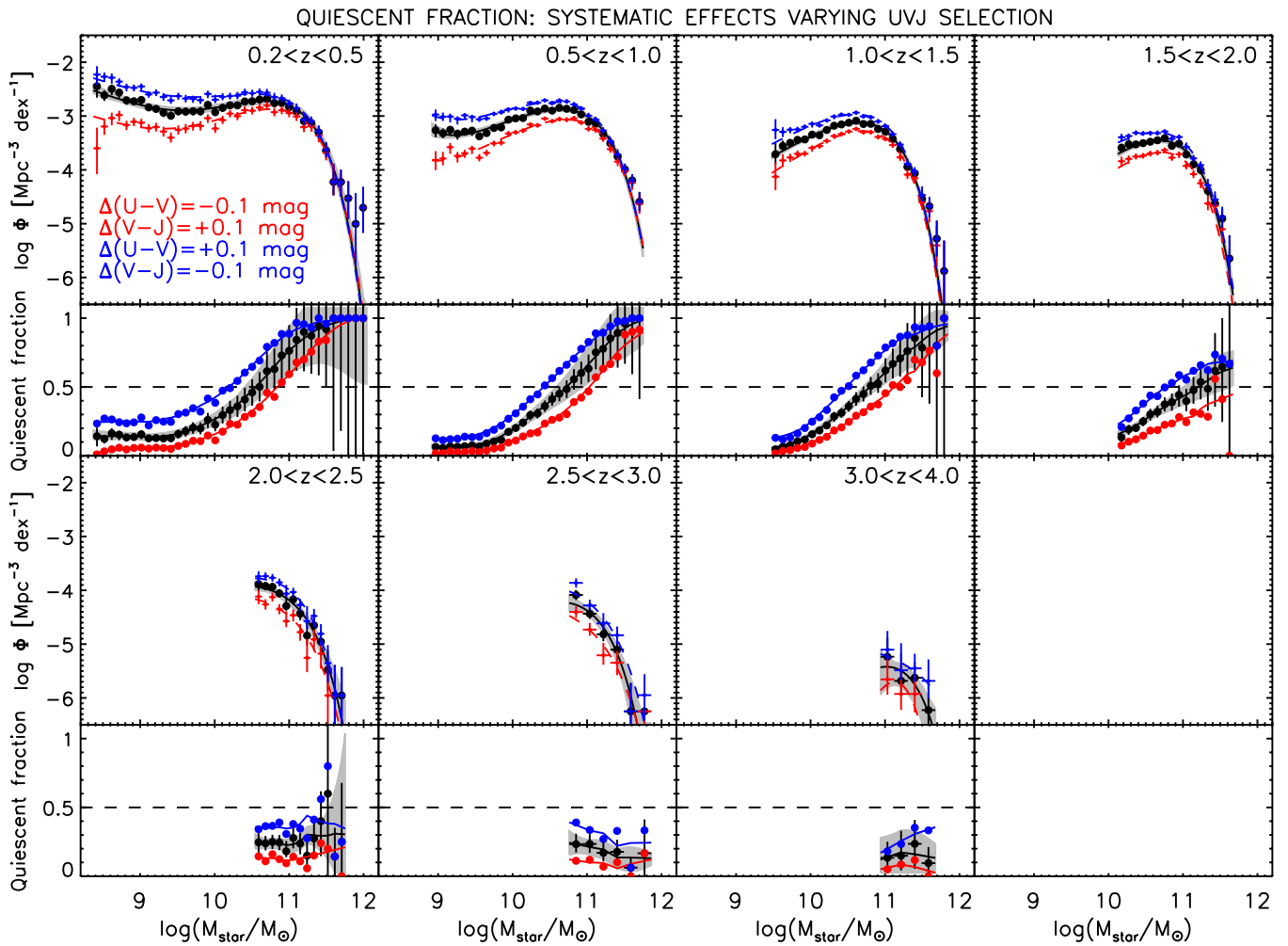


Figure 21. As in Figures 19 and 20, but in the middle panels the fraction of quiescent galaxies as a function of stellar mass is shown. Although the absolute fraction of quiescent galaxies changes with the definition of quiescence, the trend that more massive galaxies are more frequently quiescent is robust. The result that star-forming galaxies dominate the SMF at all masses at $z > 2.5$ is also robust to the definition of quiescence.

(A color version of this figure is available in the online journal.)

of the COSMOS/UltraVISTA field. In this Appendix, we make a comparison between those SMFs and the ones derived in this paper. In Figure 22, we plot both our SMFs and the I13 SMFs for the total, star-forming, and quiescent populations in the different redshift bins. In Figure 23, a comparison of the SMDs derived from the SMFs of the various populations as a function of redshift is shown.

In general, there is reasonable agreement between our SMFs and the I13 SMFs for the combined population at all redshifts, particularly at the high-mass end. There is some tension with the low-mass-end slopes, as can also be seen in the SMDs where the I13 total SMDs are systematically 0.1–0.2 dex higher than our derivation, mostly resulting from a slightly steeper low-mass end in I13, but also partially due to slightly higher overall number densities at all masses in several redshift bins.

Comparing the SMFs of the star-forming and quiescent galaxies between the surveys shows more mixed agreement than the total SMFs. In almost all redshift bins, the high-mass end of the SMFs of both types do agree reasonably well. The exceptions to this are the lowest redshift bin, $0.2 < z < 0.5$, and an intermediate redshift bin, $1.5 < z < 2.0$. The disagreement at $0.2 < z < 0.5$ is surprising and it is not obvious what its origin is. Both catalogs show excellent agreement between the

z_{phot} and the zCOSMOS spectroscopic redshifts, which are most complete for high-mass galaxies at low redshift. The difference could result from the definitions of a quiescent galaxy; however, it is surprising that it should matter as it is at the lowest redshifts where the definition of a quiescent galaxy is least ambiguous. A better understanding of this discrepancy will require an object-by-object comparison between catalogs.

The agreement at the low-mass end of the star-forming and quiescent SMFs is not as good as at the high-mass end, with generally the I13 SMFs having shallower α values for quiescent galaxies and steeper α values for star-forming galaxies. This is most likely the result of the different definitions of a quiescent galaxy between the studies. I13 define quiescent galaxies using a $NUV - M(r)$ versus $M(r) - M(J)$ color–color space, which is similar, although not identical, to the UVJ selection that we use. As we showed in the previous Appendix, if we adjust the location of the UVJ box to a more conservative cut we would produce quiescent SMFs that are in better agreement with those from I13. Likewise, I13 could most likely accommodate our SMFs if they were to move the location of their UV –optical color box to a less conservative cut.

Comparison of the SMDs in Figure 23 shows that there is reasonable agreement between the surveys for the quiescent

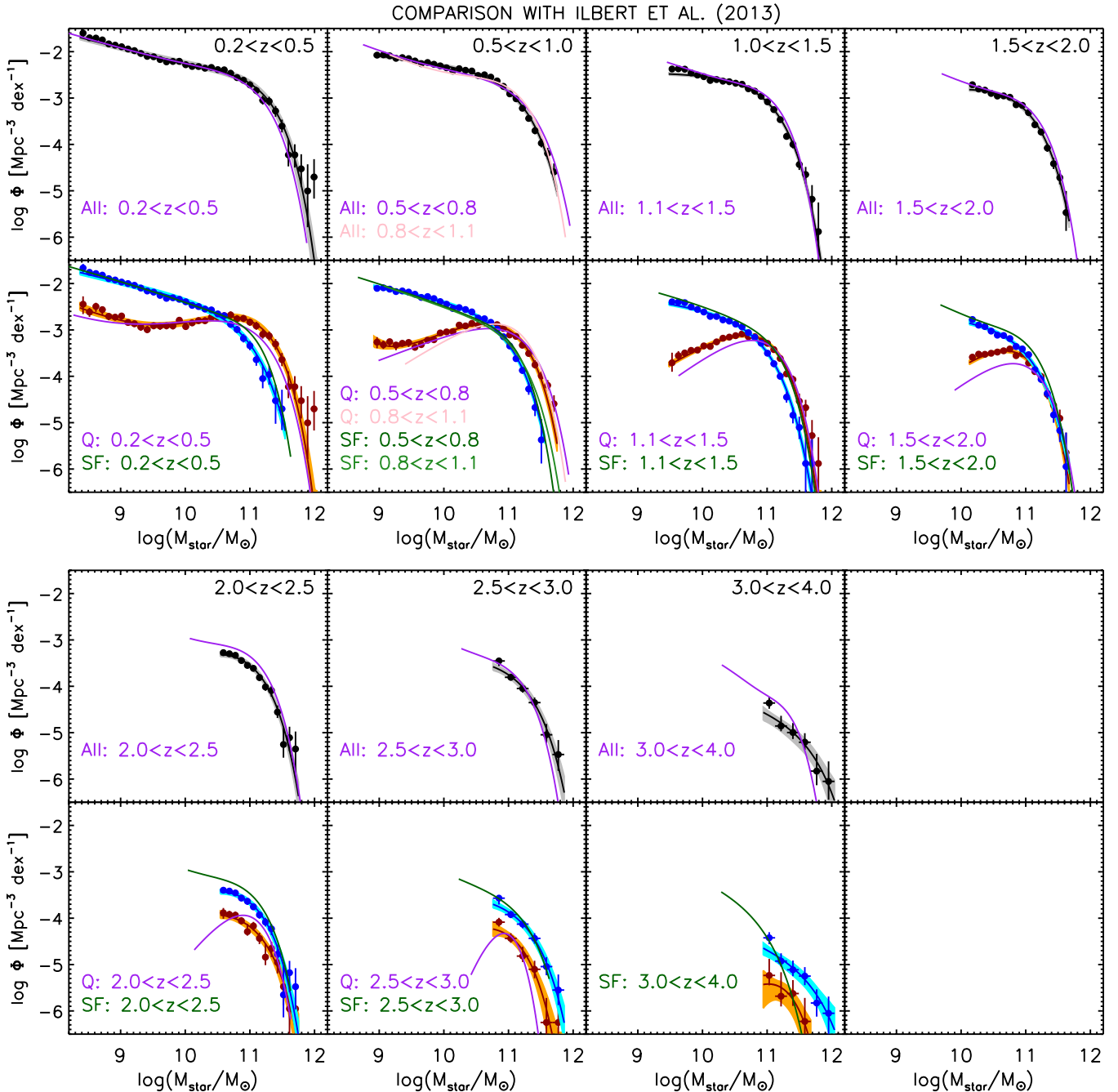


Figure 22. Comparison of SMFs of the star-forming, quiescent, and combined populations from this paper with those from Ilbert et al. (2013). The shaded regions represent the best-fit maximum-likelihood Schechter functions and the associated uncertainties and the solid points represent the $1/V_{\max}$ SMFs. The colored curves in each panel are the best-fit maximum-likelihood SMFs from Ilbert et al. (2013). The combined SMFs show good agreement in most places. There is some disagreement between the SMFs of the star-forming and quiescent populations, which likely arises from the different definitions for these used (see the text).

(A color version of this figure is available in the online journal.)

population at all redshifts. This is because α is fairly shallow so the SMD is dominated by massive galaxies. For star-forming galaxies, I13 derive SMDs that are a factor of ~ 2 higher than ours at high redshift. Again, this is partially due to the steeper α that they derive, but is also partially because their overall number densities are slightly higher at all M_{star} . It may not be a surprise that the largest difference is the low-mass-end slopes, as α is always the most difficult part of the SMF to constrain. The low-mass-end slope has frequently been a point of controversy in previous measurements of the SMFs as it is the location where the photometry is the lowest quality, hence M_{star} and z_{phot} are the least well constrained.

Overall, although there are some specific differences, the comparison between the two sets of SMFs and SMDs derived from identical data using different methods shows more consistency than discrepancy up to $z = 4$. This shows that there is a reasonable consensus in the SMFs determined with NIR-selected samples, particularly at the high-mass end where the S/N of the photometry is the highest. The comparison does illustrate two outstanding issues in the accuracy of the SMFs that warrant further investigation. First, it is clear that the definition of star-forming and quiescent galaxies needs to be defined in a careful and consistent way. A detailed study of both the UVJ diagram and the NUV –optical diagram and the locations of

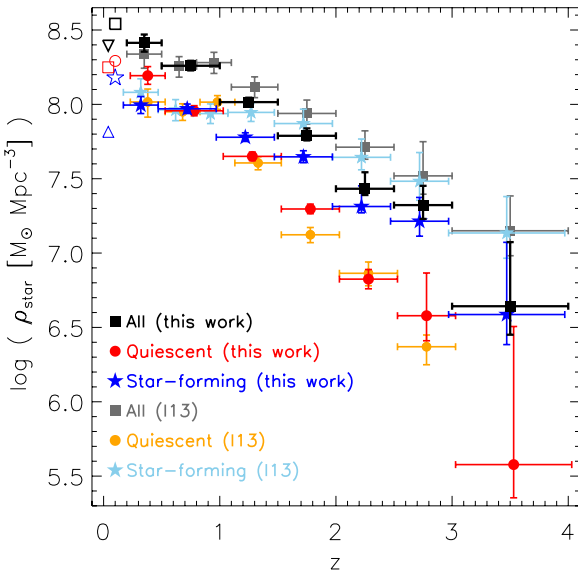


Figure 23. Comparison of SMDs of the star-forming, quiescent, and combined populations from this paper with those from Ilbert et al. (2013). In general, there is reasonable agreement at most redshifts. Notable exceptions are the SMDs in star-forming galaxies at high-redshift, where the differences are primarily due to a steeper α in Ilbert et al. (2013). There is also some discrepancy in the SMD in quiescent galaxies at low redshift and the reason for this is not immediately clear given that the data quality is best for bright galaxies at low redshift and both catalogs agree very well with the zCOSMOS spectroscopic redshifts. (A color version of this figure is available in the online journal.)

galaxies of a given SSFR in those diagrams would be useful for choosing boundaries in both that not only correspond better to each other, but also correspond to the best possible separation of star-forming and quiescent galaxies. Second, better measurements of α will be important for resolving differences in the SMDs. Given that measuring α requires pushing the data to the lowest S/Ns, it is not surprising that discrepancies between measurements at the low-mass end are common in this type of work (e.g., the discussion in Reddy & Steidel 2009). One obvious step forward in measuring α will be the DR2 UltraVISTA data, which should offer a substantial improvement in S/N for the faintest sources.

REFERENCES

- Arnouts, S., Walcher, C. J., Le Fèvre, O., et al. 2007, *A&A*, 476, 137
 Avni, Y., & Bahcall, J. N. 1980, *ApJ*, 235, 694
 Baldry, I. K., Driver, S. P., Loveday, J., et al. 2012, *MNRAS*, 421, 621
 Balogh, M. L., Baldry, I. K., Nichol, R., et al. 2004, *ApJL*, 615, L101
 Bell, E. F., McIntosh, D. H., Katz, N., & Weinberg, M. D. 2003, *ApJS*, 149, 289
 Bell, E. F., Wolf, C., Meisenheimer, K., et al. 2004, *ApJ*, 608, 752
 Bezanson, R., van Dokkum, P., van de Sande, J., Franx, M., & Kriek, M. 2013, *ApJL*, 764, L8
 Bielby, R., Hudelot, P., McCracken, H. J., et al. 2012, *A&A*, 545, A23
 Blanton, M. R., & Moustakas, J. 2009, *ARA&A*, 47, 159
 Bouwens, R. J., Illingworth, G. D., Labbe, I., et al. 2011, *Natur*, 469, 504
 Brammer, G. B., van Dokkum, P. G., & Coppi, P. 2008, *ApJ*, 686, 1503
 Brammer, G. B., Whitaker, K. E., van Dokkum, P. G., et al. 2009, *ApJL*, 706, L173
 Brammer, G. B., Whitaker, K. E., van Dokkum, P. G., et al. 2011, *ApJ*, 739, 24
 Bruzual, G., & Charlot, S. 2003, *MNRAS*, 344, 1000
 Bundy, K., Ellis, R. S., Conselice, C. J., et al. 2006, *ApJ*, 651, 120
 Calzetti, D., Armus, L., Bohlin, R. C., et al. 2000, *ApJ*, 533, 682
 Capak, P., Aussel, H., Ajiki, M., et al. 2007, *ApJS*, 172, 99
 Caputi, K. I., Cirasuolo, M., Dunlop, J. S., et al. 2011, *MNRAS*, 413, 162
 Chabrier, G. 2003, *PASP*, 115, 763
 Cole, S., Norberg, P., Baugh, C. M., et al. 2001, *MNRAS*, 326, 255
 Conroy, C., Gunn, J. E., & White, M. 2009, *ApJ*, 699, 486
 Cucciati, O., Tresse, L., Ilbert, O., et al. 2012, *A&A*, 539, A31
 Domínguez Sánchez, H., Pozzi, F., Gruppioni, C., et al. 2011, *MNRAS*, 417, 900
 Drory, N., Bundy, K., Leauthaud, A., et al. 2009, *ApJ*, 707, 1595
 Drory, N., Salvato, M., Gabasch, A., et al. 2005, *ApJL*, 619, L131
 Efstathiou, G., Ellis, R. S., & Peterson, B. A. 1988, *MNRAS*, 232, 431
 Elsner, F., Feulner, G., & Hopp, U. 2008, *A&A*, 477, 503
 Fioc, M., & Rocca-Volmerange, B. 1999, arXiv:astro-ph/9912179
 Fontana, A., Salimbeni, S., Grazian, A., et al. 2006, *A&A*, 459, 745
 Fontanot, F., De Lucia, G., Monaco, P., Somerville, R. S., & Santini, P. 2009, *MNRAS*, 397, 1776
 Förster Schreiber, N. M., Franx, M., Labbé, I., et al. 2006, *AJ*, 131, 1891
 Gehrels, N. 1986, *ApJ*, 303, 336
 González, V., Labbé, I., Bouwens, R. J., et al. 2011, *ApJL*, 735, L34
 Henriques, B., White, S., Thomas, P., et al. 2013, *MNRAS*, 431, 3373
 Hogg, D. W., Blanton, M. R., Brinchmann, J., et al. 2004, *ApJL*, 601, L29
 Hopkins, A. M., & Beacom, J. F. 2006, *ApJ*, 651, 142
 Ilbert, O., McCracken, H. J., Le Fèvre, O., et al. 2013, *A&A*, 556, A55
 Ilbert, O., Salvato, M., Le Floc'h, E., et al. 2010, *ApJ*, 709, 644
 Kajisawa, M., Ichikawa, T., Tanaka, I., et al. 2009, *ApJ*, 702, 1393
 Kauffmann, G., Colberg, J. M., Diaferio, A., & White, S. D. M. 1999, *MNRAS*, 303, 188
 Kauffmann, G., Heckman, T. M., White, S. D. M., et al. 2003, *MNRAS*, 341, 54
 Kauffmann, G., & White, S. D. M. 1993, *MNRAS*, 261, 921
 Kriek, M., Labbé, I., Conroy, C., et al. 2010, *ApJL*, 722, L64
 Kriek, M., van Dokkum, P. G., Franx, M., et al. 2006, *ApJL*, 649, L71
 Kriek, M., van Dokkum, P. G., Franx, M., et al. 2008, *ApJ*, 677, 219
 Kriek, M., van Dokkum, P. G., Labbé, I., et al. 2009, *ApJ*, 700, 221
 Kroupa, P. 2001, *MNRAS*, 322, 231
 Labbé, I., Franx, M., Rudnick, G., et al. 2003, *AJ*, 125, 1107
 Labbé, I., González, V., Bouwens, R. J., et al. 2010, *ApJL*, 708, L26
 Labbé, I., Huang, J., Franx, M., et al. 2005, *ApJL*, 624, L81
 Lee, K.-S., Ferguson, H. C., Wiklind, T., et al. 2012, *ApJ*, 752, 66
 Le Fèvre, O., Paltani, S., Arnouts, S., et al. 2005, *Natur*, 437, 519
 Leja, J., van Dokkum, P., & Franx, M. 2013, *ApJ*, 766, 33
 Li, C., & White, S. D. M. 2009, *MNRAS*, 398, 2177
 Lilly, S. J., Le Fèvre, O., Renzini, A., et al. 2007, *ApJS*, 172, 70
 Maraston, C. 2005, *MNRAS*, 362, 799
 Maraston, C., Daddi, E., Renzini, A., et al. 2006, *ApJ*, 652, 85
 Maraston, C., Pforr, J., Renzini, A., et al. 2010, *MNRAS*, 407, 830
 Marchesini, D., Stefanon, M., Brammer, G. B., & Whitaker, K. E. 2012, *ApJ*, 748, 126
 Marchesini, D., van Dokkum, P., Quadri, R., et al. 2007, *ApJ*, 656, 42
 Marchesini, D., van Dokkum, P. G., Förster Schreiber, N. M., et al. 2009, *ApJ*, 701, 1765
 Marchesini, D., Whitaker, K. E., Brammer, G., et al. 2010, *ApJ*, 725, 1277
 Martin, D. C., Fanson, J., Schiminovich, D., et al. 2005, *ApJL*, 619, L1
 McCracken, H. J., Milvang-Jensen, B., Dunlop, J., et al. 2012, *A&A*, 544, A156
 Mortlock, A., Conselice, C. J., Bluck, A. F. L., et al. 2011, *MNRAS*, 413, 2845
 Moster, B. P., Somerville, R. S., Newman, J. A., & Rix, H.-W. 2011, *ApJ*, 731, 113
 Moustakas, J., Coil, A., Aird, J., et al. 2013, *ApJ*, 767, 50
 Muzzin, A., Marchesini, D., Stefanon, M., et al. 2013, *ApJS*, 206, 8
 Muzzin, A., Marchesini, D., van Dokkum, P. G., et al. 2009a, *ApJ*, 701, 1839
 Muzzin, A., van Dokkum, P., Franx, M., et al. 2009b, *ApJL*, 706, L188
 Noeske, K. G., Weiner, B. J., Faber, S. M., et al. 2007, *ApJL*, 660, L43
 Onodera, M., Renzini, A., Carollo, M., et al. 2012, *ApJ*, 755, 26
 Papovich, C., Finkelstein, S. L., Ferguson, H. C., Lotz, J. M., & Giavalisco, M. 2011, *MNRAS*, 412, 1123
 Patel, S. G., Holden, B. P., Kelson, D. D., et al. 2012, *ApJL*, 748, L27
 Peng, Y., Lilly, S. J., Kováč, K., et al. 2010, *ApJ*, 721, 193
 Peng, Y.-J., Lilly, S. J., Renzini, A., & Carollo, M. 2012, *ApJ*, 757, 4
 Pérez-González, P. G., Rieke, G. H., Villar, V., et al. 2008, *ApJ*, 675, 234
 Pozzetti, L., Bolzonella, M., Lamareille, F., et al. 2007, *A&A*, 474, 443
 Pozzetti, L., Bolzonella, M., Zucca, E., et al. 2010, *A&A*, 523, A13
 Quadri, R., van Dokkum, P., Gawiser, E., et al. 2007, *ApJ*, 654, 138
 Reddy, N. A., & Steidel, C. C. 2009, *ApJ*, 692, 778
 Rudnick, G., Labbé, I., Förster Schreiber, N. M., et al. 2006, *ApJ*, 650, 624
 Sandage, A., Tamman, G. A., & Yahil, A. 1979, *ApJ*, 232, 352
 Sanders, D. B., Salvato, M., Aussel, H., et al. 2007, *ApJS*, 172, 86
 Santini, P., Fontana, A., Grazian, A., et al. 2012, *A&A*, 538, A33
 Schaye, J., Dalla Vecchia, C., Booth, C. M., et al. 2010, *MNRAS*, 402, 1536
 Schechter, P. 1976, *ApJ*, 203, 297
 Schmidt, M. 1968, *ApJ*, 151, 393
 Sobral, D., Smail, I., Best, P. N., et al. 2013, *MNRAS*, 428, 1128
 Stark, D. P., Ellis, R. S., Bunker, A., et al. 2009, *ApJ*, 697, 1493
 Taylor, E. N., Franx, M., van Dokkum, P. G., et al. 2009, *ApJ*, 694, 1171

- van de Sande, J., Kriek, M., Franx, M., et al. 2011, [ApJL](#), **736**, L9
van de Sande, J., Kriek, M., Franx, M., et al. 2013, [ApJ](#), **771**, 85
van Dokkum, P. G., Whitaker, K. E., Brammer, G., et al. 2010, [ApJ](#), **709**, 1018
Weinmann, S. M., Pasquali, A., Oppenheimer, B. D., et al. 2012, [MNRAS](#), **426**, 2797
Whitaker, K. E., Labb  , I., van Dokkum, P. G., et al. 2011, [ApJ](#), **735**, 86
Whitaker, K. E., van Dokkum, P. G., Brammer, G., & Franx, M. 2012, [ApJL](#), **754**, L29
White, S. D. M., & Frenk, C. S. 1991, [ApJ](#), **379**, 52
White, S. D. M., & Rees, M. J. 1978, [MNRAS](#), **183**, 341
Williams, R. J., Quadri, R. F., Franx, M., van Dokkum, P., & Labb  , I. 2009, [ApJ](#), **691**, 1879
Williams, R. J., Quadri, R. F., Franx, M., et al. 2010, [ApJ](#), **713**, 738
Wuyts, S., Labb  , I., Franx, M., et al. 2007, [ApJ](#), **655**, 51
Wuyts, S., Labb  , I., Schreiber, N. M. F., et al. 2008, [ApJ](#), **682**, 985
Zibetti, S., Gallazzi, A., Charlot, S., Pierini, D., & Pasquali, A. 2013, [MNRAS](#), **428**, 1479